HIF-dependent expression of creatine kinase brain isoform (CKB) promotes breast cancer metastasis, and blocking creatine kinase activity with cyclocreatine impairs invasion and improves the efficacy of conventional chemotherapies

Raisa I. Krutilina[1,*], Hilaire C. Playa[1,*], Danielle L. Brooks[1], Luciana P. Schwab[1], Deanna N. Parke[1], Damilola Oluwalana[1], Douglas R. Layman[1], Meiyun Fan[1], Daniel L.. Johnson[2], Junming Yue[1], Heather Smallwood[3], and Tiffany N. Seagroves[1,**]

[1]Center for Cancer Research and the Department of Pathology and Laboratory Medicine, College of Medicine, The University of Tennessee Health Science Center, Cancer Research Building, 19 South Manassas Street, Memphis, TN 38163, USA. [2]Molecular Bioinformatics Core, Office of Research, The University of Tennessee Health Science Center, 71 South Manassas Street, Memphis, TN 38163, USA. [3]Department of Pediatrics, College of Medicine, The University of Tennessee Health Science Center, 71 South Manassas Street, Memphis, TN 38163, USA.

[*]Denotes equal author contribution

[**]Corresponding author:

Tiffany N. Seagroves, Ph.D.

Rm 262 Cancer Research Bldg.

19 S. Manassas St.

Memphis, TN 38163

(901) 448-5018

tseagro1@uthsc.edu

Abstract

The oxygen-responsive Hypoxia Inducible Factor (HIF)-1 promotes several steps of the metastatic cascade. A hypoxic gene signature is enriched in triple negative breast cancers (TNBCs), which correlates with poor patient survival. Since inhibiting the HIF transcription factors with small molecules is challenging, we sought to identify genes downstream of HIF-1 that could be targeted to block invasion and metastasis. Creatine kinase brain isoform (CKB) was identified as a highly differentially expressed gene in a screen of HIF-1 wild type and knockout mammary tumor cells derived from a transgenic model of metastatic breast cancer. CKB is a cytosolic enzyme that reversibly catalyzes the phosphorylation of creatine, generating phosphocreatine (PCr) in the forward reaction, and regenerating ATP in the reverse reaction. Creatine kinase activity is inhibited by the creatine analog cyclocreatine (cCr). Loss and gain of function genetic approaches were used in combination with cCr therapy to define the contribution of CKB expression or creatine kinase activity to cell proliferation, migration, invasion, and metastasis in ER-negative breast cancers. Although tumor cell-intrinsic CKB was not essential for breast tumor cell proliferation or cell migration *in vitro*, CKB was necessary for cell invasion *in vitro* and strongly promoted tumor growth and metastasis *in vivo*. Similarly, cyclocreatine therapy repressed cell migration, cell invasion, formation of invadopodia, and lung metastasis. Moreover, in common TNBC cell line models, the addition of cCr to conventional agents, paclitaxel (Taxol) or doxorubicin, was either additive or synergistic to repress tumor cell growth.

Introduction

A major clinical challenge in breast cancer is to prevent and to treat metastatic disease. The overall survival rate of patients with metastatic breast cancer (MBC) remains dismal, irrespective of molecular subtype. Up to 30% of all patients with an early-stage diagnosis will die from metastatic disease within five years, and ~6% of patients are initially diagnosed with stage IV disease [1]. Resistance to therapeutic modalities and disease progression is characterized by the emergence of once dormant individual metastatic cells or microscopic lesions [2]. Targeting dysregulated tumor cell metabolism is a promising avenue to address drug resistance and to prolong the survival of patients with metastatic cancers [3, 4]. Several metabolic pathways that are altered in tumors relative to normal cells, including glutamine metabolism, fatty acid metabolism, and aerobic glycolysis, are linked to therapeutic resistance [4].

The hypoxic response and the oxygen-responsive Hypoxia Inducible Factor (HIF) transcription factors play an essential role in mediating these pathways in tumors. HIF-1 and HIF-2 regulate transcription of genes that fine-tune cellular metabolism, including glucose uptake, glycolysis, mitochondrial respiration, and oxidative stress, in addition to genes that control tumor cell proliferation, survival, or apoptosis [5-7]. HIF-1 has also been directly implicated as a mediator of chemoresistance in tumor cells through the regulation of metabolic input [6, 8, 9]. Moreover, hypoxia in general, and HIFs, specifically, play a critical role in promoting breast cancer metastasis and therapeutic resistance [6, 8-13]. Over-expression of either HIF-1α or its 123-gene transcriptional “core signature”, independently

correlates with decreased survival in breast cancer patients [14-16]. We previously demonstrated in a transgenic mouse model of MBC that develops lung metastasis with 100% penetrance (MMTV-PyMT; FVB/Nj strain) [17] that HIF-1α is essential for primary tumor growth and lung metastases that originate from the mammary fat pad. Specifically, HIF-1α deletion in the tumor epithelial cells reduced tumor size by 60%, lung metastasis by >90%, and tumor-initiating (cancer stem-like cell) potential by >35-fold [13].

Despite clear connections to the promotion of tumor progression and metastasis, targeting the HIFs with small molecules is challenging. Although several HIF chemical inhibitors have been described, most do not discriminate between HIF-1 or HIF-2, and they indirectly, rather than directly, impact HIFα stability/activity [18]. One exception is the first in class HIF-2 antagonist PT2385 (Peleton Therapeutics, Inc.) that binds allosterically to HIF-2α, but not to HIF-1 α, preventing heterodimerization and binding to DNA [19]. PT2385 prolonged disease control in clinical trials for renal clear cell carcinoma [20]. Furthermore, deletion of either HIFα subunit is deleterious to normal development [21], suggesting potential toxicity of HIF inhibitors to normal cells. Finally, differential, or even competing roles, for HIF-1α and HIF-2α in tumorigenesis have been reported, as reviewed in [22].

To address these obstacles in developing HIF inhibitors for clinical use, we screened for genes downstream of HIF-1 that were differentially expressed in response to genetic knockout of HIF-1α, with the rationale that these targets may be more amenable to therapeutic intervention. HIF-1 wild type (WT) and knockout

(KO) PyMT cells grown at normoxia or hypoxia were analyzed by microarray profiling. Genes previously implicated to modulate cellular metabolism and/or invasion that were down-regulated in response to HIF-1 KO, and for which chemical inhibitors had been previously identified, were prioritized for biological validation. One differentially-expressed gene that met this profile was the enzyme creatine kinase, brain isoform (CKB).

CKB is a member of a family of four creatine kinase enzymes [23], which reversibly transfer a high-energy phosphate group between ATP and creatine, generating phosphocreatine and ADP. Phosphocreatine is an essential local energy reservoir that highly metabolic tissues exploit to rapidly re-generate ATP from ADP in a CK-dependent manner, including muscle, the brain, and the gastrointestinal tract [24, 25]. The CK system is necessary to maintain a high ratio of ATP/ADP and to prevent local acidification near cellular ATPases. Both functions are relevant to tumors, which rely on aerobic glycolysis to produce energy and exist in an acidic microenvironment [8]. The cytosolic creatine kinases (*CKB* and creatine kinase, muscle, *CKM*), the ubiquitous mitochondrial creatine kinase (*CKMT1*), and the creatine transporter (*SLC6A8*) are each direct HIF-responsive genes [26]. Neither CKB nor CKMT1 are essential for development since single or compound knockout mice are viable and fertile, although the double knockout mouse exhibits decreased body size and severe defects in behavior and learning [27, 28]. The cytosolic creatine kinases, CKB and CKM, function as obligate homo-or-heterodimers (CK-BB, CK-MM, or CK-MB, respectively). The dimerization of CKB is dependent upon a cysteine near the active site. When this

cysteine is mutated to serine (C283S), the mutant will dimerize, but the CK-BB enzyme is essentially “kinase-dead” with a 96% reduction in the production of phosphocreatine [29].

Compared to normal cells, CKB is over-expressed in a variety of solid tumors [25], including breast cancer, colorectal cancer, and ovarian cancer [30-34]. Up-regulation in tumor cells has also been confirmed in proteomic screens of prostate, lung, and HER2+ breast cancers [35-38]. CK-BB serum levels are elevated in breast cancers and are predictive of an increased risk of death, particularly in CKB+, estrogen receptor (ER)- tumors [34]. More recently, in HER2+ breast cancers, HER-2 signaling was shown to promote ABL kinase phosphorylation of mitochondrial CKMT1 at tyrosine 153 to prevent its proteolytic destruction [39], providing ATP to fuel growth. None of the other creatine kinase isoforms were found to be modulated by ABL.

Targeting creatine kinases is underdeveloped as an anticancer strategy targeting cellular metabolism. In the 1990s, several creatine analogs, including cyclocreatine (1-Carboxymethyl-2-iminoimidazolidine, cCr), were shown to inhibit tumor growth, complemented by tolerable side effect profiles in rodents, reviewed in [25]. Cyclocreatine has the most similar substrate kinetics to creatine, but unlike creatine, which is actively transported into cells by the creatine transporter (SLC6A8), cCr passively enters cells and likely crosses the blood-brain barrier [40, 41]. In a rat mammary adenocarcinoma model cCr monotherapy (0.5-1.0 g/kg/day, IP) repressed tumor growth [42]; however, the impact on metastasis was not tested. Cyclocreatine is known to inhibit tumor cell motility *in vitro*, which is

reversible by the addition of exogenous creatine [43]. In a colon cancer xenograft model, CKB mediated the metastatic potential of cancer cells by acting as a secreted kinase to produce phosphocreatine, which accumulated in the stroma. The phosphocreatine was then imported into tumor cells via the creatine transporter (SLC68A) to promote CK-dependent survival of tumor cells while in the circulation, as well as their colonization and expansion in the liver [44]. Either knockdown of CKB in the colon cancer cells or implantation of an osmotic pump releasing cyclocreatine into the peritoneum repressed liver metastasis [44]. More recently, in pancreatic adenocarcinoma, CKB was identified as a mechanosensitive transcriptional target of yes-associated protein 1 (YAP); stiff substrate increased CKB mRNA and protein levels and production of ATP to facilitate collective cell invasion and chemotaxis [45]. These results build upon prior *in vitro* observations that suggested that CKB supplies the ATP necessary for actin reorganization, and that found CKB protein localizes in a spatially restricted manner in migrating cells [46-48]. Overall, these observations suggest a direct link of creatine kinase activity not only to tumor cell metabolism but also to cellular motility necessary for the metastatic cascade. Overall, the creatine arm of metabolism may be a key player downstream of the HIFs to promote metastasis in solid tumors.

Based upon these observations, we tested if CKB mediates breast cancer metastasis to the lung, a predominant site of metastasis in women diagnosed with triple-negative breast cancer (TNBC) [49-51]. Expression of CKB was HIF-dependent at the mRNA and protein levels when cells were exposed to either

normoxia or hypoxia. Upon shRNA knockdown of *Ckb*, there were no changes in cell proliferation or in wound healing *in vitro*; however, cell invasion through Matrigel was reduced and total intracellular ATP production decreased. In contrast, over-expression of CKB enhanced chemotaxis and cell invasion whereas cCr treatment blocked wound healing, invasion, and formation of invadopodia. Analysis of cellular metabolism revealed that knockdown of *Ckb* repressed both mitochondrial respiration and glycolysis. *In vivo*, either deletion of *Ckb* in the tumor epithelial cells or treatment with cCr following tail vein injection strongly repressed lung metastasis in host mice. These data demonstrate that creatine metabolism is essential for HIF-dependent lung metastasis in breast cancer. Finally, pairing cCr with conventional cytotoxic chemotherapies was either additive or synergistic to repress TNBC cell line growth. In sum, we conclude that breast tumor cell-intrinsic expression of CKB is required to mediate cellular metabolism and to promote cell invasion and metastasis in ER-negative breast cancer models and that addition of cCr to conventional cytotoxic agents represses tumor cell growth over monotherapy.

Materials and Methods

Chemicals. Cyclocreatine (cCr) was purchased from either Sigma-Aldrich (#377627, 98% purity) or Cayman Chemical Company (cat# 20649, Ann Arbor, MI, >95% purity). Doxorubicin was purchased from Sigma-Aldrich (cat.# D1515, >98% purity), and paclitaxel (>99.5% purity) was purchased from LC Laboratories (cat.#

P-9600, Woburn, MA). For use *in vitro*, cCr stock was freshly diluted to 50 mM in complete growth medium immediately before use. Paclitaxel (Taxol) and doxorubicin (DOX) were prepared in DMSO as 20 mM and 5 mM stocks, respectively, and stored at -20°C; thawed stocks were serially diluted in DMSO to prepare working stocks for *in vitro* assays. For use *in vivo*, cCr was dissolved to ~1.92 mg/mL into sterile 0.9% saline using gentle heat, sterile filtered, and then stored in 50 mL aliquots at -20ºC. At the time of treatment, the frozen aliquot was heated to ~50ºC, transferred to a sterile glass evacuated vial, and stored protected from light in a thermos heated to 37ºC. cCr was immediately injected into mice (IP) at a final dose of 1.0 g/kg/day, seven days a week. Sterile saline (0.9%) served as the vehicle control.

PyMT mammary tumor epithelial cell (MTEC) cells. HIF-1 wild-type (WT) and knockout (KO) MTECs derived from the mouse mammary tumor virus (MMTV)-driven polyoma virus middle T antigen (PyMT) transgenic mouse harboring *floxed* alleles of *Hif1a* were established and maintained in culture as in [13]. This model is ER/progesterone receptor (PR)-negative [13]. Briefly, cells were grown in DMEM/F12 media supplemented with 2% FBS (Life Technologies, cat.# 16-000-044) and 15 mM HEPES. All cells were cultured at normoxia in a standard CO_2 incubator (5% CO_2) or exposed to hypoxia (0.5% O_2, 5% CO_2) in a multi-gas incubator (Sanyo, Osaka, Japan). Unless otherwise stated, cells were exposed either acutely (≤ 6h) or chronically (16-24h) to hypoxia. Cells were routinely

screened for mycoplasma using the MycoAlert kit (cat.# LT07-418, Lonza, Basel, Switzerland).

RNA extraction and gene expression microarray analysis. HIF-1 WT and KO PyMT cells were seeded into 6-well plates in DMEM/F12 medium (n=6 wells/genotype) supplemented with 2% FBS and 15 mM HEPES. At ~80% confluence, plates were left at normoxia or were transferred to hypoxia (0.5% O_2) for 6 hours, a period when HIF-1 transcriptional activity peaks for classic target genes in this model [13]. At harvest, individual wells were washed three times with cold PBS, scraped, and cells pelleted and flash frozen. Total RNA was prepared from partially thawed cell pellets using RNABee reagent (Tel-Test, Friendswood, TX). Three independent replicate total RNA samples with RNA integrity numbers (RIN) >9.0 were compared per genotype per oxygen tension using microarrays. Total RNA was hybridized to the MouseRef-6v1.1 Expression BeadChip Kit (Illumina, San Diego, CA) at the UTHSC Molecular Resource Center of Excellence (MRC) core facility. Raw data were transformed to the $\log_2$-scale, and normalized log-scale intensity values were analyzed for differential expression using Expander software [52]. All genes with a mean fold-differential ≥ 2.0, and with a *p*-value <0.05 among technical replicates per genotype per condition are included in differentially-expressed gene lists (HIF-1 WT normoxia vs. HIF-1 WT hypoxia, HIF-1 WT vs. HIF-1 KO, normoxia and HIF-1 WT vs. HIF-1 KO, hypoxia; refer to gene lists in **Supplementary Tables S1-S3**, respectively). Raw data can be accessed from the GEO database (GSE183694).

Real-time PCR. Total RNA was converted to cDNA using the High-Capacity cDNA Reverse Transcription Kit (Applied Biosystems, Waltham, MA). Quantitative, real-time PCR (qPCR) was performed using primer and probe sets designed by the Universal Probe Library (UPL) Assay Design Center software and qPCR was performed using the LC480 real-time PCR instrument under default cycling conditions (Roche Applied Science, Indianapolis, IN, USA; all primers are listed in **Supplemental Table S4**). Crossing point (Cp) values were normalized based on the expression of the integrator complex subunit 3 (*Ints3*) for mouse genes or cyclophilin A (*PPIA*) for human genes. To compensate for any changes in epithelial content in total RNA extracted from PyMT whole tumors between genotypes, since only the tumor epithelium is deleted for *Hif1a*, *Ints3*-normalized Cp values were also normalized to *Krt18* (cytokeratin 18).

Immunofluorescence of cultured cells. Cells were cultured to sub-confluence in multi-well chamber slides (ibidi, Gräfelfing, Germany). At harvest, cells were washed with cold PBS and then fixed with 4% paraformaldehyde/PBS, washed and stored at 4°C. Cells were permeabilized with 0.1% Triton-X, washed, and then blocked for at least 1h at room temperature (RT) with buffer containing both BSA and normal serum from the host species of the secondary antibody. Primary antibodies to CKB, to cortactin, or to alpha-tubulin were incubated at 4°C overnight in blocking buffer, following by washing in PBS containing Tween-20 (PBST). Cortactin and tubulin were detected with anti-IgG secondary antibodies for 1h at RT (either AlexaFlour-488, or AlexaFluor-594, Life Technologies). Tertiary

amplification was used to detect CKB; after primary antibody, cells were incubated with donkey anti-rabbit-biotin-X-IgG secondary antibody (cat. #A16027, Life Technologies, 1;400), washed, and then incubated with Alexa-Fluor-594-conjugated streptavidin. Prior to mounting, cells were counterstained with DAPI, washed with PBS, the excess PBS was removed, and then ibidi mounting medium was added. Slides were stored, covered, in the dark at RT until imaging on a Nikon inverted ECLIPSE Ti2 fluorescent microscope. Images were captured using NIS-Elements software and the enhanced intensity projection module was used to compile images from multiple z-stacks. A list of all antibody reagents is included in **Supplementary Table S5**.

Protein extraction and western blotting. Whole cell extracts (WCE) and high-salt enriched WCE (HS-WCE) fractions were prepared as in [13]. To detect HIF-1α, HS-WCE (5 μg input) was resolved on a 3-8% Tris-Acetate gel system (Life Technologies). To detect CKB, WCE (20-40 μg input) was resolved on either 4-12% Tris-Bis or 10% Tris-Bis BOLT gels (Life Technologies, Carlsbad, CA) and transferred onto polyvinylidene fluoride (PVDF) or PVDF Fluorescent (PVDF-FL) membrane (Millipore, Burlington, MA). To confirm efficient transfer and/or equivalent loading, membranes were stained with Ponceau S (Sigma, St. Louis, MO) and scanned. Membranes were then de-stained prior to blocking with either 5% non-fat dry milk (NFDM)/TBST for enhanced chemiluminescence (ECL) using the Millipore Immobolin ECL reagent, or with Odyssey blocking buffer (LiCor Biosciences,) for near-infrared (NIR) detection. Membranes were probed with

primary antibodies followed by extensive washing and incubation with anti-rabbit whole IgG secondary antibodies conjugated to either HRP (Jackson Immunologicals, West Grove, PA) or to NIR fluorophores (LiCor Biosciences, Lincoln, NE). Antibody complexes were detected by ECL and membranes exposed to film, or membranes were directly imaged using the LiCor Odyssey or Azure Sapphire infrared imaging systems. Western blotting reagents are reviewed in **Supplementary Table S5**. To normalize for protein loading, membranes were stripped with ReBlot plus mild stripping buffer (Millipore), then re-blocked in 5% NFDM and incubated with antibodies to ß-tubulin or PARP and developed as described above. Alternatively, .tiff images of Ponceau-S-stained membranes were analyzed by ImageStudio densitometry analysis (LiCor Biosystems) to agnostically quantitate whole lane signal.

Creatine kinase enzymatic activity assay. WCE prepared as described above were analyzed using a creatine kinase activity assay reagent as per manufacturer instructions (cat.#: C712-39, Pointe Scientific, Canton, MI). Enzymatic activity was normalized to total protein content as determined by the Bio-Rad Laboratories Bradford assay (cat.#: 5000002, Hercules, CA).

Patient database mining. Datasets were analyzed using The Cancer Genome Atlas (TCGA) database [53] and Kaplan-Meier (KM)Plotter [54]. The level of *CKB* mRNA expression in breast tumor subtypes was derived from the TCGA data portal (http://cancergenome.nih.gov/). Level three normalized data derived from

Illumina RNASeqv2 data were used to compare mRNA expression, and samples were stratified by tumor subtype based on the PAM50 method. Plots were generated using and *p*-values ≤ 0.05 (ANOVA with Bonferroni correction) were considered significant (last accessed October 4, 2016). For regression-free survival (RFS) analysis, KMPlotter was stratified by CKB (200884_at) mRNA or protein (P12277) expression in breast cancer patients (last accessed February 3, 2021).

Promoter analysis and chromatin immunoprecipitation (ChIP) assays. The mouse and human *CKB* proximal promoters (-2000 to +500 bp) were scanned for the presence of putative functional hypoxic response elements (HREs) using the Transcription Factor Matrix (TFM) Explorer algorithm using weight matrices available from JASPER and TRANSFAC. Primers were designed to putative independent HREs in both the murine and human promoters, as well as to non-HRE sequences in the corresponding promoter regions (**Supplementary Table S6**). PyMT HIF-1 WT and KO cells and MCF7 EV (pLKO.1-puro) or shHIF1A transduced cells described in [55] were cultured at 21% (normoxia) or 0.5% O_2 (hypoxia) for 6-24 hours and fixed with 1% formaldehyde for 12 min. DNA was sheared to 500 bp length by sonication using a Diagenode Bioruptor set to high, with a 30-second burst followed by 30 seconds of cooling for 10 minutes. ChIP was performed using primary antibodies against HIF-1α or rabbit IgG, as a control for non-specific antibody binding using methods described in [56]. qPCR was performed on all samples using LightCycler 480 SYBR Green master mix. Input

DNA (non-IP enriched) values were used to normalize each ChIP DNA fractions' C_p value to the input DNA fraction C_p value to account for chromatin sample preparation differences ($\Delta C_{tNormalized\ ChIP}$). The normalized ChIP fraction C_p values were then adjusted for based on the normalized IgG IP fraction C_p value [$\Delta\Delta C_t$ = ($\Delta C_{tNormalized\ ChIP}$ - ($\Delta C_{tNormalized\ IgG}$)]. Assay site IP fold enrichment above the sample-specific background was then calculated as $2^{(-\Delta\Delta Ct)}$. As a positive control, a previously validated functional HRE identified in the *Vegf* promoter was also used in PyMT ChIP assays [57]. As a positive control for human ChIP assays in MCF-7 cells, a previously validated functional HRE identified in the *EPO* promoter [58] was used.

Generation of PyMT *Ckb* knockdown cells. PyMT HIF-1 WT cells were used to create *Ckb* stable shRNA knockdown (KD) via lentiviral transduction. To identify an efficient targeting construct, a *Ckb* shRNA library containing 3 independent *Ckb* targeting sequences screened by the RNAi Consortium (TRC) and individually cloned into the pLKO.1-puro vector was purchased from Open Biosystems (Gene ID: 12709, clone IDs: TRCN0000024659, "sh59", TRCN0000026460, "sh60" and TRCN0000024661, "sh61"; **Supplementary Table S7**). Approximately one million cells were transfected with each pLKO.1-shRNA containing plasmid (4 μg) by nucleofection with kit T and program setting 24 (Nucleofector, Lonza). Two of the three pLKO.1 plasmid constructs, sh59 and sh61 produced >70% knockdown by western blot (**Supplementary Fig. S2A-B**). Lentivirus particles for pLKO.1-empty (empty vector, EV), and the pLKO.1-puro sh59 and sh61 constructs were produced

by the UTHSC Viral Vector Core. HIF-1 WT PyMT cells were transduced with lentivirus particles at a multiplicity of infection of 50. Puromycin (2 μg/mL) was added 72h later to select for transduced cells and a “pool” of surviving clones (representing several hundred colonies) was established for each shRNA construct. Stably transduced lines were maintained in culture with normal PyMT growth media plus 1 μg/mL puromycin. Puromycin was removed from cells at least 4 days before biological assays or treatment with cCr.

PyMT cell proliferation assay by WST-1. PyMT cells were grown in normoxic culture (ambient air; 5% CO_2) or hypoxic culture (0.5% O_2; 5% CO_2) in medium buffered with 15 mM HEPES. On the day before enumeration, 20,000 cells were plated into 96-well plates in normal growth medium. The medium was changed 24 h post-plating, which coincides with the time zero time point and the first cell harvest for cell number analysis (t=0), and medium was not replenished for the duration of the experiment. All assays were plated in triplicate per genotype/oxygen tension/time point. Background absorbance detected in blank wells was subtracted from sample wells and raw data normalized to the EV controls (% maximal proliferation vs. EV). For the treatment of EV and sh61 cells with cCr to generate a dose-response curve, cCr was dissolved to a 75 mM stock in growth media containing 2% FBS. At 24 h post-seeding, growth media without drug or media containing increasing doses of cCr (from 2 mM to 50 mM) was replaced. Cells were incubated with drug for an additional 96 h and then analyzed for viability using the WST-1 assay at endpoint (Chemicon, cat.#2210, Burlington,

MA). Background absorbance detected in blank wells was subtracted from sample wells and growth inhibition was measured as the change in absorbance over time, normalized to the vehicle control for each cell line (set to 100%).

Wound healing assays. PyMT EV, HIF-1 KO, and *Ckb* KD cells were plated in 12-well plates in growth medium (30,000 cells/well; n=3 replicate wells per genotype). Cells were grown for 48 h to 100% confluence. Each well was scratched by a 1 mL tip in a vertical and horizontal direction to create a cross in the center of each well. After scratching, cells were washed with medium to remove the detached cells and replaced with fresh growth medium. The time of initial scratch was stipulated as time t=0 h. Pictures of scratches (a cross in the center of each well) were taken at 100x magnification at times 0, 8, 24, 32, 48, 56, and 72 h post-scratch. Analysis was performed by loading images into ImageJ. Open wound area was calculated as the percentage open wound area to the total area in the field of view.

Additional wound healing assays were performed using the IncuCyte S3 live-cell imaging system and the WoundMaker tool. PyMT EV cells were pre-incubated for 24 h with 25 mM cCr in growth media supplemented with 2% FBS. Cells were plated into 96-well format Image Lock microplates (Sartorius, Göttingen, Germany) at a density of 40,000/cells/well (n=8 technical replicates/condition) such that cells would be 100% confluent approximately 24 h post-plating. The WoundMaker tool was used to create a uniform 700-μM scratch/well, the wounds were gently washed and growth medium containing either

vehicle (no cCr) or 25 mM cCr was applied. As a control, wounded EV cells that were not pre-treated with cCr were then either exposed to vehicle or to cCr (25 mM). Images were obtained every 2-4 h for 24 h and raw data were analyzed using the IncuCyte total wound area algorithm and then exported into Prism 9.0.

Transient ectopic expression of CKB in MDA-MB-231 cells. MDA-MB-231-NR (NucLight red) cells (generously provided by Sartorius; RRID:CVCL_DF48) were transfected with FuGene HD reagent (Promega, Madison, WI) with 3 μg of either an empty vector pCMV-6-Entry C-terminal Myc and DDK-tagged plasmid OriGene, cat# PS100001, Rockville, MD) or pCMV-6-CKB-Myc-DDK TrueORF Gold plasmid (cat#RC203669, NCBI accession: NM_001823) and selected with neomycin (2 mg/mL) for up to 72 h before use in invasion and chemotaxis assays.

Invasion assays. PyMT EV, HIF-1 KO, and *Ckb* KD cells were first gradually weaned from growth medium supplemented with 2% FBS to 0.5% FBS as in [13]. Cells weaned to 0.5% FBS were then cultured 18 h in serum-free DMEM/F-12 medium. The next day, 25,000 cells were plated onto control inserts or Matrigel-coated transwell inserts (BD Biosciences, San Jose, CA) and attracted to wells containing DMEM/F12 medium supplemented with 5% FBS. Cells were plated in triplicate per genotype/oxygen tension. The mean cell invasion index corrected for random migration was calculated at 48 h post-seeding as per the manufacturer's instructions.

To determine if re-expression of CKB in HIF-1 KO PyMT cells would rescue invasion, vector control, or HIF-1 KO cells stably transfected to express mCKB were gradually weaned to 0.5% FBS and then plated at a density of 40,000 cells into transwells and attracted to 5% FBS for 48 h. MDA-MB-231 transiently transfected cells (empty vector or +mCKB) were serum-starved overnight before plating onto inserts and then attracted to medium supplemented with 10% FBS for 24 h. For studies comparing normoxia to hypoxia, changes in PyMT cell invasion are expressed as the fold change relative to the invasion index observed for HIF-1 WT cells cultured at normoxia (set to a fold change = 1.0). Otherwise, all other data are expressed as the % of invading cells (invading cells/total cells plated).

Intracellular ATP Assay. Intracellular ATP levels were compared using the high sensitivity ATP Bioluminescence Assay HS II kit (cat. #11699709001, Sigma). PyMT cells were grown to 80% confluence prior to incubation in normoxic or hypoxic culture for 24 h. All cells were plated in triplicate per genotype/oxygen tension. At 24 h cells were harvested and lysed using the lysis reagent provided in the kit supplemented with a protease and phosphatase cocktail inhibitor (cOmplete EDTA-free tablets, Sigma, cat#4693132001). Luciferase reagent was added 1 second (s) prior to a 10 s integrated reading on a single-tube luminometer. A blank (reagent only) reading was obtained and subtracted from all sample readings. An ATP standard curve was generated to plot bioluminescence versus molarity on a log-log scale and used to calculate intracellular ATP concentrations in samples. DNA concentrations for each individual sample were measured using a Qubit®

fluorometer (Life Technologies), and all ATP concentrations were normalized to total DNA per sample.

Seahorse bioanalyzer assays. PyMT cells were harvested using a dispase: trypsin mixture without EDTA as in [13] followed by DNaseI treatment. Following washing and resuspension in growth media, cells were strained to remove clumps and then counted by hemacytometer and seeded into Seahorse XFe-96 sensor microwell plates (Agilent Technologies, Santa Clara, CA) at an optimized density to produce near confluence within 18 h. The next day, the plate was transferred to the Department of Pediatrics Bioenergetics Core for metabolic assays using the Seahorse XFe96 Extracellular Flux Analyzer. First, cells were switched to an XF base medium (non-buffered DMEM without phenol red). XF media was supplemented with L-glutamine (2 mM) for the XF Cell Glyco Stress test or with glucose (10 mM), L-glutamine (2 mM), and sodium pyruvate (1 mM) for the XF Cell Mito Stress test. Cells were equilibrated for 1 h prior to analysis of extracellular acidification rate (ECAR) or the oxygen consumption rate (OCR). After each plate run, the number of cells per well was quantified using CyQUANT dye (Thermo Scientific) for normalization. Metabolic rates were calculated using the Seahorse XF real-time report generator, and the data were then imported into Prism 9.0 for statistical analysis.

Chemotaxis assays. MDA-MB-231-NR cells transiently transfected (48h) with empty vector (EV, pCMV-Entry) or to express mCKB were seeded at a density of

1,000 cells/per of a 96-well IncuCyte ClearView chemotaxis plate (cat. #4582, Sartorius) (n=4-6 technical replicates/cell line), which allows cell tracking through optically clear membrane inserts for direct visualization of migration in real-time. Cells were exposed to a reservoir containing DMEM +10% FBS as the chemoattractant. Plates were imaged every 2 h and the chemotaxis analysis software tool was used to quantify cell migration through the insert pores. Raw data were normalized for initial plating density prior to export to Prism 9.0 for statistical analysis.

Cytotoxicity assay using the IncuCyte S3 live-cell imager. PyMT cells were seeded at 5,000 cells per well in 96-well dishes and allowed to adhere overnight. The following day, growth medium (vehicle control) or cCr was added. A 10 μM working stock solution of CytoTox Green reagent (Sartorius, cat.# 4633) was made fresh as per the manufacturer's instructions and added to each well at a final concentration of 250 nM. The plate was placed into the S3 instrument and cells were allowed to equilibrate for approximately one hour before initiation of imaging; each well was imaged in three locations every 4 h for a total of 48 h. At the experimental endpoint, the phase and fluorescent masking software algorithms were applied to analyze the data, then the results were exported to Prism 9.0 and normalized to corresponding initial seeding density as measured by phase contrast. Data are representative of two independent biological experiments with n=6 technical replicates/time point/cell line.

Cell cycle analysis. PyMT EV or sh61 KD cells were plated into 6-well dishes and when sub-confluent were treated with vehicle control or with 25 mM cCr for either 24 h (added 24 h prior to experiment endpoint) or 48 h. At harvest, cells were washed with PBS then trypsinized. Trypsin was inactivated with media containing 10% FBS. Cell pellets were washed twice with cold PBS and then re-suspended in 500 μL ice-cold 70% ethanol and the final volume was increased to 5 mL prior to storage at 4°C. On the day of cytometry analysis, samples were washed twice again with PBS and then treated with RNaseI. Setting aside an unstained sample as a gating control, propidium iodide was added to a final concentration of 50 μg/mL and incubated at 37°C for 15 min prior to analysis on the BioRad ZE5 flow cytometer at the UTHSC Flow Cytometry and Cell Sorting Core. Raw data were exported to ModFit for analysis (n=3 technical replicates/genotype/time point, with at least duplicate biological replicates per genotype per time point).

PyMT primary tumor generation. All animal studies were carried out in adherence to the NIH Principles of Laboratory Animal Care and protocols as approved by the Institutional Animal Care and Use Committee at the University of Tennessee Health Science Center. To generate PyMT mammary tumors, EV, HIF-1 KO, HIF-1 WT + sh59 (sh59), and HIF-1 WT + sh61 (sh61) *Ckb* knockdown (KD) cells were injected into the cleared inguinal mammary fat pads of 3-4 week old FVB/Nj female recipients. Cultured MTECs were dissociated into single cells with 0.05% trypsin-EDTA, diluted 1:1 (v:v) in growth factor reduced Matrigel (BD Biosciences, Franklin Lakes, NJ):Hank's balanced salt solution (HBSS), and

injected into the cleared inguinal mammary fat pads of recipient mice (50,000 cells per 10 µl volume) with a 26-gauge PT2 needle mounted onto a Hamilton glass syringe. Recipients were palpated one or two times per week, and tumor outgrowths were measured with digital calipers to calculate volume as described in [13]. In a subsequent experiment, primary tumors were generated and then resected in a survival surgery under anesthesia when tumors grew to a volume of ~500 mm^3, and the mice were allowed to survive until moribund due to lung metastasis.

Tissue immunohistochemistry and immunostaining quantification. Harvested tumors were bisected with a razor and fixed for 8-24 h in 10% neutral-buffered formalin. Paraffin-embedded specimens were sectioned (5-7 µM) onto positively charged slides. Antigen retrieval was performed in 1x citrate buffer (pH 6.0) in a pressure cooker. Slides submerged into the heated citrate solution were allowed to completely cool to RT. Endogenous peroxidase was blocked by submersion of slides into 3% H_20_2/MeOH for 20 minutes, followed by washing in water then PBS. All slides were blocked in 10% normal serum/PBST at least 1 h at RT before incubation of primary antibody overnight in humid chambers at 4°C. Slides were washed then stained with the ABC Elite anti-rabbit kit (cat. # PK-6100, Vector Labs, Burlingame, CA) per manufacturer's instructions and then developed using DAB Impact substrate (cat. #SK-4105, Vector Labs) and counterstained in hematoxylin (cat.# H3401, Vector Labs). Slides were coverslipped with a xylene-based mounting medium, allowed to dry, then whole slides were digitally scanned

using a 3DHISTECH PANORAMIC slide digitizer. Staining intensity was analyzed by pixel counts using built-in densitometry algorithms optimized for nuclear or cytoplasmic localization (3D Histech, Ltd. software package, Budapest, Hungary). Following masking to exclude necrotic areas, whole tumor sections were analyzed per slide. The background was set using adjacent sections that were developed without primary antibodies. Primary antibodies included: Ki67, activated caspase-3, and CD31. Antibody reagents are listed in **Supplementary Table S5**.

Tail vein assays in PyMT mice. PyMT EV, sh59, and sh61 *Ckb* KD cells prepared as a single cell suspension were injected directly into the circulation via the tail vein at a density of $1x10^6$ cells per 100 µl/HBSS. Mice were sacrificed after 21 days, and lungs were inflated with 10% NBF via the trachea and then post-fixed in NBF overnight. Paraffin-embedded sections (5-7 µm) representing every 100 µm of lung tissue were obtained for each paraffin block, and all sections were stained with H & E. The individual H & E-stained section containing the highest number of metastases per recipient, as evaluated by counting each slide under a light microscope at 50x original magnification, was used to determine the mean number of metastases per genotype as in [13]. To test cCr efficacy, PyMT EV cells were injected into the tail vein as described, and cells were allowed to seed the lungs for 24 h. cCr dosing regimen was based on [42]. Mice were treated with vehicle (0.9% saline, daily, IP) or cCr (1g/kg, daily, IP) beginning 24 h post tail vein injection. In one cohort, daily treatment with 1 g/kg/day of cCr was delayed until 7

days post-injection (after lung micro-metastases had formed). On day 21, all mice were euthanized to collect lungs for histopathology.

Human breast cancer cell lines. MDA-MB-231 and MDA-MB-453 TNBC cells obtained from the Fan laboratory via the American Type Culture Collection (ATCC) were grown in DMEM-Hi medium supplemented with 10% FBS (cat.# FB-01, Omega Scientific, Tarzana, CA), MDA-MB-468 TNBC cells obtained from the Fan laboratory via ATCC were grown in DMEM/F-12 medium supplemented with 10% FBS and BT549 TNBC cells obtained directly from ATCC were grown in RPMI medium supplemented with 10% FBS. All cell lines were authenticated at the University of Arizona Genetics Core. Spent media collected from near confluent cells was routinely screened for mycoplasma using the Lonza MycoAlert kit.

Invadopodia assays. Glass coverslips were coated with OregonGreen-gelatin (cat. #G13186, ThermoFisher) as outlined in [59]. Coated coverslips were transferred to ultra-low adhesion 24-well culture dishes, which facilitated cells adhering to the gelatin rather than the plate surface. Cells (BT549, 12,000/well or MDA-MB-231, 15,000/well) were seeded onto coverslips in growth media containing a reversible MMP inhibitor, batimistat (10μM; cat. # SML0041, Sigma) and incubated overnight. The next day, the media was replaced with fresh growth media to allow invadopodia formation to begin, or cCr (25 mM) was also added. Plates containing seeded coverslips were placed into the IncuCyte S3 live-cell imager and simultaneously imaged in both the green fluorescence and phase

channels, capturing sixteen images per coverslip per time point. The green fluorescent area was normalized to seeding density per image and graphed as a ratio of change over time in Prism 9.0. At the end of the imaging period, optimized for each individual cell line, coverslips were fixed and processed as described for immunofluorescence and stained slides were mounted directly onto glass slides using ProLong Gold Antifade curing mounting media (cat.# P36930, ThermoFisher) and imaged on the Nikon ECLIPSE Ti2 microscope as previously described.

Human TNCB cell growth inhibition assays using the IncuCyte S3 live cell-imager. The day before measuring growth, cells were seeded at a density such that the assay would begin the next day at ~20% confluence (8,000 cells for MDA-MB-468, 12,000 cells for MDA-MB-453, and 5,000 cells for MDA-MB-231 and BT549 cells). To begin the assay, growth media used to seed cells was removed and each dilution of chemotherapy drug, or the vehicle control, was spiked into media also containing either IncuCyte Nuclight Rapid Red (cat.# 4717, Sartorius) or Miami Green (cat.# EMI001, Kerafast, Boston, MA) to enumerate cell nuclei. Plates were imaged in an IncuCyte S3 instrument every 2-4h, depending on the proliferation rate of each cell line. Growth inhibition percentage was calculated relative to vehicle controls, which was calculated by measurement of red or green fluorescent units localized to the nucleus after applying the IncuCyte masking algorithm to enumerate cell count. Data were exported to Prism 9.0 and normalized to initial seeding density. Drug synergism was calculated using the isobole method

[60], wherein a combination index of >1.0 indicates antagonism, an index of ~1.0 is additive and an index of <1.0 suggests synergism.

Statistical analysis. Unless otherwise stated, all raw data were entered into Prism 9.0 (Graph Pad, San Diego, CA) and analyzed using one-way or two-way ANOVA, followed by multiple pairwise comparison tests (*t*-tests). When the standard deviation was not similar between the two groups, Welch's correction was applied. On all graphs, the mean ± SEM is shown. Significance was determined with a 95% confidence threshold as indicated by asterisks defined as: *$p<0.05$, **$p<0.01$, ***$p<0.001$, ****$p<0.0001$.

Results

Ckb is a HIF-1α dependent target gene in metastatic breast cancer cells

We have previously shown that tumor cell-intrinsic HIF-1α expression is required for mammary tumor growth and metastasis to the lung in the MMTV-PyMT mouse model of breast cancer [13]. In order to identify HIF-dependent genes that mediate metastasis and that may be more amenable to therapeutic intervention than the HIF transcription factors, we performed microarray profiling using both HIF-1 WT and KO PyMT cells cultured at normoxia or acute hypoxia. Several hundred differentially-expressed genes were identified that met cutoff criteria for the following comparisons: 1) HIF-1 WT normoxia vs. HIF-1 WT hypoxia; 2) HIF-1 WT normoxia vs. HIF-1 KO normoxia; 3) HIF-1 WT hypoxia vs. HIF-1 KO hypoxia (refer to **Supplementary Tables S1-S3**). Many of the differentially expressed genes down-regulated in either normoxic or hypoxic HIF-1 KO cells, including *Egln3* (*Phd3*), aldolase C (*Aldoc*), and *Pdk1*, are known HIF-1α target genes involved in cancer cell migration and invasion, tumor initiation and growth, and metastasis [61-64].

The enzyme creatine kinase brain isoform (*Ckb*) was one of the top HIF-dependent, but not hypoxia-dependent, differentially expressed genes. *Ckb* was down-regulated in normoxic HIF-1 KO cells by 13.4-fold (p=0.0093) (**Supplementary Table S2**). Following acute hypoxia exposure, *Ckb* expression in HIF-1 WT cells was 16.42-fold higher than in HIF-1 KO cells (p=0.0002) (**Supplementary Table S3**). However, *Ckb* was not differentially expressed in HIF-1 WT normoxic vs. hypoxic cells, which suggested that *Ckb* mRNA levels depend

more on HIF-1α expression than hypoxia stimulus (**Supplementary Table S1**). Based on CKB's well-described role in regulating energy metabolism, and prior studies using creatine analogs that function as chemical inhibitors of the creatine kinase pathway, including cyclocreatine (cCr) [65, 66], we sought to determine if *Ckb* plays a key role in mediating breast cancer metastasis to distant organs. Our array profiling screen was purposefully performed in HIF-1 WT and KO cells derived from the PyMT transgenic model, since, when backcrossed to the FVB/Nj strain, 100% of transgenic mice will develop lung metastasis [67]. Moreover, we have demonstrated that recipient mice implanted into the mammary fat pad with cultured HIF-1 WT PyMT tumor epithelial cells also develop lung metastasis with 100% penetrance [13].

To validate the *Ckb* expression changes observed by microarray profiling, an independent set of PyMT HIF-1 WT and KO cultured cells was exposed to normoxia or to hypoxia, for 6h or for 24h. By real-time PCR (qPCR), a significant decrease in *Ckb* mRNA expression levels was observed in normoxic HIF-1 KO cells compared to WT cells at either 6 h or 24 h of normoxia, with a mean 7.44-fold decrease in expression. Comparing HIF-1 WT and KO cells cultured at hypoxia, there was a more modest decrease in expression in HIF-1 KO cells of ~1.7-fold (**Figure 1A**).

We next investigated whether CKB is a direct HIF transcriptional target in PyMT cells and in human MCF-7 cells, which express CKB in an estrogen-responsive manner [68]. Two consensus hypoxia-response elements (HREs) were identified in both the murine *Ckb* and human *CKB* promoters (**Supplementary**

Figure S1A). Chromatin immunoprecipitation (ChIP) assays were performed using PyMT HIF-1 WT and HIF-1 KO cells or MCF-7 cells that were transduced with either parent the pLKO.1-puro backbone (empty vector, EV) or with pLKO.1-shRNA to *HIF1A* as detailed in [69]. HIF-1α was recruited to both the -1326 and -1835 HRE sites in PyMT WT cells relative to HIF-1 KO cells (**Supplementary Figure S1B**), with a fold change in site occupancy of 11.5-fold or 4.6-fold, expressed as the ratio of HIF-1 WT over HIF-1 KO occupancy at each site relative to the corresponding genotype IgG IP controls, respectively (**Supplementary Figure S1B**). Enrichment of HIF-1α at the -258 site of the *CKB* promoter in MCF-7 EV cells relative to shHIF1A cells was also confirmed, with a fold change in site occupancy of 1.8-fold in EV over shHIF1A; no enrichment at the -935 site was observed (**Supplementary Figure S1C**). Therefore, in either an estrogen-receptor negative [PyMT, [13]] or in an ER+ breast cancer cell line, MCF-7, HIF-1 directly regulates CKB mRNA expression, as was first reported in the colon [26]. In addition, as expected, knockdown (KD) of *HIF1A* in MCF-7 cells significantly down-regulated *CKB* mRNA levels measured by qPCR (**Supplementary Figure S1D**).

The relationship of oxygen tension to CKB protein levels in PyMT cells was then compared by western blotting. Similar to mRNA data, exposure of cells to hypoxia for 24 h did not induce CKB protein in HIF-1 WT cells above normoxic (0h) levels (**Figure 1B**). Reduced *Ckb* expression in HIF-1 KO cells was also shown by immunofluorescence (**Figure 1C**). CKB appeared to localize to the cytoplasm in a perinuclear pattern, as well as to the nucleus. Although its predominant role is believed to be in the cytoplasm, CKB nuclear localization and association with the

nuclear matrix have also been reported in colon cancer cells [30]. CKB levels were also compared in PyMT HIF-1 WT and HIF-1 KO end-stage tumors derived from tumor cells implanted into FVB/Nj recipients [13]. A reduction in *Ckb* mRNA levels, normalized for epithelial content using keratin 18 (*Krt18*), (**Figure 1D**), and a reduction in CKB protein levels in whole tumor extracts were also observed (**Figure 1D**). It should be noted that the whole-cell extracts prepared from tumors contain proteins expressed by both tumor epithelial cells and by the stroma, likely minimizing the total reduction in CKB since only the tumor epithelium lacks HIF-1α expression.

CKB mRNA is expressed in all breast cancer subtypes and expression is correlated with shortened regression-free survival in breast cancer patients

The Cancer Genome Atlas (TCGA) database was queried to compare normalized *CKB* mRNA expression in breast cancer patients stratified by the PAM50 subtype (**Figure 1F**). *CKB* is expressed in all breast cancer subtypes, with significant enrichment in patients diagnosed with HER2+ breast cancer relative to basal-like or luminal A subtypes. Comparing regression-free survival (RFS) using KMPlotter, high *CKB* mRNA expression levels correlated with a higher probability of RFS, regardless of subtype (**Figure 1F**). In basal breast cancers, this hazard ratio increased (**Figure 1F**). Although limited breast cancer cases were available to query at the protein level, high levels of CKB also significantly correlated with reduced RFS (**Figure 1G**).

Knockdown of *Ckb* does not impact cell proliferation or wound healing but impairs cell invasion through extracellular matrix

To determine if CKB impacts metastasis and, therefore, reduces overall survival, we generated *Ckb* loss of function models in PyMT cells using shRNA-mediated KD. Three independent shRNAs were cloned into the pLKO.1-puro backbone and were tested by transfecting the viral backbone into HIF-1 WT PyMT cells. Two shRNAs produced >70% knockdown at both the mRNA and protein levels (herein referred to as sh59 and sh61, **Supplementary Figure S2A**). Recombinant lentivirus particles were then produced from each shRNA construct to transduce HIF-1 WT PyMT cells, resulting in >70% reduction of *Ckb* mRNA and protein as compared to either HIF-1 WT or empty vector (HIF-1 WT+ EV) control transduced cells (**Figure 2A-B** and **Supplementary Figure 2A-2B**). By both qPCR and western blotting, the sh61 *Ckb* KD pool showed the greatest reduction in CKB levels (**Figure 2A-B**). In addition, deletion of *Ckb* did not affect HIF-1α expression (**Supplementary Figure S2C**).

To determine if loss of only one isoform of creatine kinases (CKB), of the two cytoplasmic creatine kinases and the two mitochondrial isoforms [25], impacted total creatine kinase (CK) enzymatic activity, CK activity (CK^{act}) levels were compared using extracts from PyMT EV and *Ckb* KD cells exposed to normoxia or hypoxia. Measuring CK^{act} was also important to predict sensitivity to cyclocreatine (cCr). It has been previously shown that tumor cell responsiveness to cyclocreatine is dependent upon total CK^{act}. Cells with very low CK^{act} (0.01-0.05 U/mg protein) were reported to be resistant or refractory to cCr *in vitro*, whereas

cell lines that have high creatine kinase activity were found to be cCr-responsive (>0.10 U/mg protein) [70, 71]. Independent of oxygen tension, loss of CKB reduced CK^{act} 3-fold in PyMT cells, decreasing from ~0.3 U/mg protein in EV cells to ~0.1 U/mg protein in sh59 and in sh61 KD cells (**Figure 2C**).

Cell proliferation over time was compared in PyMT EV and *Ckb* KD cells cultured at either normoxia or hypoxia. At normoxia, there was a slight, but significant, decrease in growth rate in the sh61 KD cells, beginning at 48 hours (**Figure 2D**). However, at hypoxia, cell proliferation was significantly decreased in the sh61 KD cells only at 24 hours (**Figure 2E**). In contrast, there were no significant differences in proliferation observed between EV and sh59 KD cells. Overall, deletion of *Ckb* had minor effects on PyMT cell proliferation *in vitro*, similar to the effects we previously observed for *Hif1a* deletion in PyMT cells [13].

CKB regulates cell motility in astrocytes and fibroblasts and in pancreatic cancer cells via local ATP production [45, 47]. Therefore, we next compared breast cancer cell motility using the wound healing assay. There was no significant difference in wound closure between PyMT EV control cells and either the sh59 or sh61 *Ckb* KD cells; in contrast, HIF-1 KO cells migrated significantly slower at all time points (**Figure 2F**). In contrast, when assayed for invasion potential in a transwell assay using inserts coated with Matrigel, there was a significant inhibition of invasion for each PyMT *Ckb* KD pool compared to EV cells. These effects were initially observed at normoxia, but were more pronounced during hypoxic culture, with a >20-fold reduction in invasion between EV and sh61 KD cells and >10-fold reduction between EV and sh59 KD cells (**Figure 2G**).

Loss of CKB represses cellular metabolism

As expected based on CKB's well-described role in metabolism, PyMT *Ckb* KD cells produced significantly less intracellular ATP than EV control cells when cultured at either normoxia or hypoxia (**Figure 3A**). Next, EV, sh59, and sh61 KD cells were characterized for metabolic activity using a Seahorse bioanalyzer. Either sh59 or sh61 KD cells showed reductions in the extracellular acidification rate (ECAR), a measure of glycolytic activity (**Figure 3B-3D**). At the peak ECAR activity for EV cells, glycolysis was significantly repressed for each *Ckb* KD pool (**Figure 3C**), whereas only sh61 KD cells showed a reduction in glycolytic capacity compared to EV cells (**Figure 3D**). Non-glycolytic acidification was also reduced in each KD pool (**Figure 3E**). These results are consistent with prior observations in ovarian cancer cells that CKB plays a key role in glycolysis [72]. In contrast, relative to EV cells, only the sh61 KD pool, which had the highest deletion efficiency of CKB (**Supplementary Figure S2**), showed deficits in the oxygen consumption rate (OCR), a readout of oxidative phosphorylation (**Figure 3F**). Both basal respiration levels and maximum respiration activity were reduced in the sh61 KD pool (**Fig. 3G-H**). ATP production rates estimated by Seahorse analysis were significantly reduced in both shRNA KD pools relative to EV cells (**Figure 3I**).

Ectopic CKB expression promotes, whereas cyclocreatine treatment represses, ER-negative breast cancer cell migration and invasion

To determine if re-expression of CKB in HIF-1 KO PyMT cells would rescue invasion, mouse CKB (mCKB) was transfected into HIF-1 KO cells and selected

for stable expression. The percentage of cells capable of invading through ECM increased in response to CKB re-expression, from 50.4% in the vector only control to 89.19% (**Figure 4A**). Next, we ectopically expressed CKB in a highly invasive TNBC cell line model, MDA-MB-231 cells. MDA-MB-231 cells do not express detectable levels of CKB protein by immunostaining (data not shown) or by immunoblotting (**refer to Figure 7A**). However, following 72 h of transient transfection of mCKB plasmid, the mean percentage of invading cells increased from 33.3% to 87.5% (**Figure 4B**). Similar results were obtained with cell lines selected to stably express mCKB (data not shown). Next, MDA-MB-231-NucLight Red (NR) cells, in which nuclei were labeled with a red dye to allow for screening in a high-throughput chemotaxis assay, were transiently transfected with vector control or +mCKB. Cells were exposed to reduced serum overnight (2% FBS) and then seeded into ClearView plates with defined pore size and spacing to view cell movement towards 10% FBS in real-time. Over-expression of mCKB in 231 cell\s dramatically increased chemotactic potential (**Figure 4C**).

To test whether treatment with cyclocreatine (cCr), a creatine analog, could mimic loss of CKB function, EV and sh61 *Ckb* KD PyMT cells were treated with increasing concentrations of cCr for 96 h and growth inhibition evaluated by the WST-1 assay. Although we had expected to observe that cCr sensitivity would be reduced in *Ckb* KD cells, the growth inhibition curves were almost identical between PyMT EV and sh61 cells. The estimated IC_{50} dose of cCr in EV and sh61 cells at 96 h was 13.73 ± 4.33 mM and 16.43 ± 2.98 mM, respectively (**Table 1**). Importantly, since 15 mM and 25 mM cCr doses were used in shorter term

biological assays (24-48 h exposure), we ruled out that these doses induce extensive cell death in either EV or KO PyMT cells. The intensity of CytoTox Green dye incorporation over time and endpoint assay images are shown in **Supplementary Figure S3A-B**. On an area basis, the basal level of cell death is higher in HIF-1 KO PyMT cells than EV cells (@t=0h of cCr exposure).

We next tested the efficacy of cCr anti-metastatic activity in a high-throughput wound assay. Either pre-treatment of PyMT EV cells with cCr prior to seeding in the assay, or adding cCr only after the scratch was applied, inhibits wound healing (**Figure 4E**). The most potent repression of healing occurred when cells were pre-treated with cCr 24 h prior to the wounding assay and then cCr was re-added for the duration of wound healing. However, cCr pre-treatment before wounding, without adding additional cCr post-scratch, was also sufficient to significantly delay wound healing (**Figure 4E**). Similar to results observed by Papalazarou et al. in pancreatic cancer cells [45], the addition of cCr to PyMT EV cells also represses invasion through ECM in transwell assays (**Figure 4F**). Overall, small molecule inhibition of the CK pathway through cyclocreatine treatment mimics loss of CKB function.

The chemotherapeutic potential of cCr is also related to its ability to block cell cycle progression. Short-term treatment with cCr has reversible effects on the cell cycle, whereas long-term treatment (several days) leads to tumor cell death [73]. To determine the effect of cCr treatment after 24 h and 48 h on the cell cycle, PyMT EV and sh61 KD cells were stained with propidium iodide and subjected to FACS analysis. EV cells treated with cCr accumulated in the G1 phase after 24 h,

with a corresponding reduction in the percentage of cells in the S-phase, and these results were exacerbated at 48 h as very few cells were detected in the S-phase **(Figure 4G**). sh61 KD cells also showed an increase in cells in the G1 phase and a decrease of cells in the S-phase; however, the differences between 24h and 48h of cCr treatment on PyMT cell cycle progression were negligible (**Figure 4G**).

Loss of *Ckb* in PyMT mammary tumor epithelium significantly represses primary tumor growth and inhibits lung metastases

To ascertain the effects of *Ckb* knockdown *in vivo*, we compared primary tumor growth of PyMT EV, HIF-1 KO, sh59 KD, and sh61 KD cells over time following transplant into the inguinal mammary fat pads of FVB/Nj recipient females. As we reported previously [13], HIF-1 KO PyMT cells exhibit a significant delay in tumor onset and a decrease in mean tumor volume that is maintained over time. In contrast to expectations based on *in vitro* cell proliferation results (**Figure 2D-E**), the tumor growth rate was similar between HIF-1 KO and each *Ckb* shRNA pool (**Figure 5A**). There was no significant difference in mean tumor volume between each shRNA pool. At day 35 post-transplant, the mean tumor volume of EV cells was ≥1000 mm^3, whereas all other genotypes had reached a maximum mean volume of ~200 mm^3. At tumor harvest on day 34, there was also a significant difference in tumor wet weight among the EV, HIF-1 KO, sh59, and sh61 genotypes (**Figure 5B**). To investigate if loss of *Ckb* impacted overall survival, in an independent experiment, all tumors were resected at a similar volume of ~750 mm^3, and animals were housed until moribund due to lung metastases. Animals

previously bearing shRNA KD tumors survived >2x longer than recipients of EV cells (7.5 weeks vs. 3.5 weeks median survival, HR= 3.681 by log-rank test, **Figure 5C**). Tumor sections from all genotypes were then immunostained with antibodies to either Ki67 to enumerate cell proliferation, to anti-activated caspase-3 to enumerate apoptosis, or to CD31 to enumerate microvessel density. Whole tumors, excluding necrotic regions, were subjected to digital scanning and densitometry-based quantification of tumor area positive for the markers of interest. Likely because the PyMT EV tumors were highly necrotic, the percentage of positive area for Ki67+ cells was higher in all of the smaller tumors (HIF-1 KO, sh59, and sh61, **Figure 5D**). As expected in response to HIF-1 KO, CD31 levels were decreased relative to EV, whereas a reduction in CD31 was only significant in sh61 KD tumors relative to EV tumors (**Figure 5E**). Approximately 9.8% of the EV tumor area was apoptotic. In contrast, very low levels of apoptosis were observed in the HIF-1 KO tumors (0.77%). Relative to KO tumors, more caspase staining was detected in both sh59 KD (3.68%) and sh61 KD (5.1%) tumors (**Figure 5F**).

Deletion of *Ckb*, or systemic treatment with cyclocreatine, blocks lung metastasis following tail vein injection

To explore if *Ckb* knockdown also blocks latter stages steps of the metastatic cascade, PyMT EV, sh59, or sh61 KD cells were injected directly into the circulation via the lateral tail vein, and lungs were harvested 21 days later. The lungs of all mice injected with EV cells were filled with large metastases visible to

the naked eye, whereas no surface metastases were observed for the sh61 KD cells (**Figure 6A**). When metastases were enumerated from H&E-stained lung sections, a strong repression of metastases in both shRNA *Ckb* KD pools was observed relative to EV cells, but there was no significant difference between the two *Ckb* KD pools (**Figure 6A**).

Next, we determined if treatment with cCr inhibits lung colonization or the growth of established lung micro-metastases. PyMT EV cells were injected into the tail vein and allowed to seed the lungs for 24 h. After 24 h, mice received daily treatment with cCr at a dose of 1 g/kg or vehicle (0.9% saline) IP for 21 days. Whereas the surface of lungs from vehicle-treated mice was filled with metastases, very few metastases were visible in the cCr cohort (**Figure 6B**). Surface lung metastases were enumerated; the majority of mice treated with vehicle developed metastases (7/8, or 87.5%) and 5/8 mice (62.5%) treated with saline developed >100 lesions. In contrast, zero metastases were observed in 5/7 mice in the cCr cohort (71.4%) and 2 mice in each cohort developed fewer than 50 metastases (χ^2 analysis, $p < 0.05$). These results were replicated in an independent tail vein experiment, in which a third cohort was added and administration of cCr therapy was delayed by 7 days, a time when lung micro-metastases have formed in this model, such that therapy was given for an additional 14 days. If mice were treated with cCr beginning at day 1 post-injection, the mean number of metastases per lung was 8.4 versus 96.8 in the saline-treated group. In contrast, approximately 50% fewer metastases were detected (a mean of 46.6) if cCr therapy was initiated on day 7 after micro-metastases had already formed (**Figure 6C**). Moreover, there

were no detectable macro-metastases in the day 1 cCr cohort, versus 3.8 in the saline group or 1.4 in the day 7 cCr cohort (**Figure 6D**). Over the course of daily treatment, mice did not lose body weight and they did not develop any other gross symptoms of toxicity. There was no significant difference in body weight whether animals were treated daily with cCr for 21 days (day 1 cCr group) or daily for 14 days (day 7 cCr group) (**Figure 6E**).

Combination of cyclocreatine with paclitaxel or doxorubicin is more effective than monotherapy in human TNBC cell lines

In a broad panel of cancer cell lines, cCr represses cell growth with similar efficacy as conventional agents, including cyclophosamide, doxorubicin, or 5-FU [42, 70, 71, 74]. *In vivo*, in a rat mammary adenocarcinoma model implanted into female Fisher 344 rats, tumor growth delay was enhanced when cCr (1g/kg, IV or IP) was paired with either cyclophosphamide, doxorubicin, or 5-FU [42]. Similar results were observed in this model when rats were fed chow supplemented with 1% cCr (weight: weight) [75]. In pancreatic cancer, and in myeloid leukemia, cCr monotherapy inhibits not only primary tumor growth but also metastasis to distant organs [45, 76]. Finally, in HER2+ trastuzumab-sensitive or -resistant breast cancer models, pairing cCr with traszutumab represses cell growth via inhibition of the ubiquitously expressed mitochondrial CK isoform (CKMT1) [39]. Based on these observations, we sought to specifically determine in ER-negative breast cancer cell line models using a formal isobole method [60] if cCr therapy was

additive to, or synergistic with, paclitaxel (Taxol) or doxorubicin (DOX), two common cytotoxic agents used to treat stage IV breast cancer.

First, we compared CKB expression levels in a panel of breast cancer cell lines representing various molecular subtypes by western blotting (**Figure 7A** and **Supplemental Figure S4**). MDA-MB-231 and SUM-159 (TNBC) and T47D (ER+, luminal B) cell lines did not express detectable levels of CKB, whereas CKB was expressed at varying levels in the other cell lines screened. CKB protein was the most abundant in MDA-MB-453 cells, a commonly used TNBC model [77], which also expresses low levels of HER2+ protein, although not at a level that meet sthe clinical cutoff for HER2-amplification [78] [79]. CKB was moderately expressed in MDA-MB-468 and in BT549 TNBC cells (**Figure 7A**); BT549 cells had similar CKB expression levels as observed in the murine HIF-1 WT PyMT cells (**Figure 1B** and **Figure 7A**). AU565 (HER2+), CAMA1 (ER+, luminal B), HCC2157 (TNBC), and HCC70 (TNBC) also expressed moderate levels of CKB. MDA-MB-436 (TNBC) cells expressed relatively low levels of CKB protein (**Supplemental Figure S4**).

Three TNBC cell line models were chosen for the evaluation of cCr efficacy as a monotherapy or in combination with paclitaxel (Taxol) or DOX, including, MDA-MB-468 (CKB moderate), BT549 (CKB moderate), and MDA-MB-453 (CKB high). The BT549 model was also selected because these cells readily form invadopodia *in vitro* [80]. The estimated IC_{50} doses of cCr and each chemotherapy were determined by phase confluence assays using the IncuCyte live-imager while in the presence of nuclear dyes to label cell nuclei (**Table 2**). Isobole assays were

used to determine if combination therapy was likely to be additive or synergistic; these results are summarized in **Table 3**.

In MDA-MB-468 cells, a combination of 10 mM cCr with 25 mM Taxol was synergistic (combination index, CI=0.52), efficiently inhibiting cell growth over time (**Figure 7B**). For DOX, 100 nM repressed growth by ~50%, but the addition of cCr to DOX further inhibited cell growth over time (**Figure 7C**); this combination was additive. In contrast, in BT549 cells, cCr was synergistic with either a 5 nM or a 25 nM dose of Taxol (**Figure 7D**), but no significant change in cell growth was observed when cCr was paired with DOX; in fact, isobole studies suggested antagonistic effects of this combination (CI>1.0) (**Figure 7E, Table 3**). In MDA-MB-453 cells, which are the most sensitive to cCr (**Table 2**), as expected based on high CKB protein expression (**Figure 7A**), the combination of either Taxol (**Figure 7F**) or DOX (**Figure 7G**) with cCr was synergistic at the IC_{50} doses of either agent (CI=0.95 and 0.77, respectively). It has been previously reported that combining cCr with Taxol enhances microtubule stability, leading to the synergistic killing of MCF-7 (ER-positive) cells in an anti-proliferative mechanism [81]. To establish if this relationship is also observed in ER-negative breast cancer cells, MDA-MB-468 cells were immunostained for alpha-tubulin. Whereas treatment with cCr slightly disrupted the microtubule network and Taxol stabilized microtubules, as expected, the addition of cCr to Taxol further stabilized tubulin networks in a pattern consistent with prior observations in MCF-7 cells [81] (**Supplementary Figure S4**). The molecular mechanisms of the observed additive effects of cCr in combination with DOX require further investigation.

Cyclocreatine represses, and ectopic expression of CKB enhances, the formation of invadopodia

To determine if CKB regulates invasion activity in part through the formation of invadopodia, two TNBC models that form invadopodia in culture were used, MDA-MB-231 and BT549 cells, since our PyMT cells do not form invadopodia (data not shown). Standard invadopodia assays were employed in which invadopodia are characterized by the loss of fluorescent gelatin which has been deposited onto glass coverslips prior to cell seeding, in addition to the presence of cortactin overlapping areas of gelatin loss [59]. We optimized protocols to image the loss of gelatin over time by imaging coverslips submerged in media into 12-well dishes using the IncuCyte S3 live-cell imaging system (**Figure 7H**). Representative experiments of two independent coverslips simultaneously imaged in the IncuCyte system revealed that treatment of BT549 cells with cCr inhibited loss of Oregon Green-conjugated gelatin over time (52 h), whereas ectopic expression of CKB in MDA-MB-231 cells stimulated the loss of gelatin over 24 h (**Figure 7H**). Loss of gelatin and the presence of cortactin in areas where invadopodia had formed were validated by immunofluorescence at the end of the imaging periods (**Figure 7I**; BT549 images are shown in **Supplementary Figure S5A**.). We also immunostained for CKB in endpoint invadopodia in MDA-MB-231 +mCKB cells. Representative images comparing empty vector and +mCKB cells revealed that CKB protein was detectable at the edges of invadopodia, in addition to its cytoplasmic and nuclear localization pattern (**Supplementary Figure S5B**).

Discussion

Although multiple roles for HIF-1α in mediating breast cancer phenotypes are well-defined [12, 13, 55, 82-87], many individual HIF-1α-dependent genes remain to be characterized for the biological role they play in tumor progression and metastasis among various solid tumor subtypes. We identified creatine kinase brain isoform (CKB) as a HIF-1α-dependent transcriptional target gene necessary for primary tumor outgrowth and lung metastasis in a commonly used transgenic model of metastatic breast cancer, MMTV-PyMT. Moreover, by mining breast cancer patient datasets, higher *CKB* mRNA or protein levels were found to be prognostic for relapse-free survival (RFS) across all molecular subtypes. The likelihood of RFS was further decreased for patients diagnosed with basal-like breast cancers. Our results are particularly relevant to those breast cancer subtypes that exhibit high constitutive expression of HIF-1α and HIF-1 target genes, including basal-like and HER2-enriched tumors [53, 88]. Based on these initial observations, we focused our studies on understanding the function of CKB in ER-negative models of breast cancer.

HIF-dependent, but not hypoxia stimulus-dependent, regulation of *Ckb* mRNA and protein levels was observed in cultured PyMT cells. Since most breast cancers and their metastases overexpress HIF-1α [89], and since $ER^{-negative}$/basal-like cancers show the highest enrichment of a HIF-dependent transcriptional program [53], no hypoxic stimulation may be needed to induce expression of CKB in ER-negative breast cancers. In addition, since HIF protein stabilization can be induced independently of hypoxia by several growth factor signaling pathways,

such as EGF and HER2, as reviewed in [90], the HIF-1-dependent, but not hypoxia-induced, expression of CKB in TNBC may also be mediated through these pathways. Finally, cell stressors such as low glucose, change in pH, and the production of reactive oxygen species (ROS), all increase HIF-1α expression [91], and could up-regulate CKB expression independent of hypoxia.

In breast cancers, like the epithelium of the colon [26], CKB is a direct HIF transcriptional target gene. We have demonstrated that PyMT HIF-1 KO cells and KO tumors express much lower levels of both *CKB* mRNA and protein. Interestingly, while CKB levels are highly HIF-1α dependent in PyMT tumor cells, neither mRNA nor protein levels changed in response to acute or chronic hypoxia. These results are in contrast to ER+ MCF-7 breast cancer cells in which we observed that *CKB* mRNA levels increase in response to either 6h or 24 h of hypoxic exposure by ~2.5-fold or 8.0-fold, respectively. Chromatin immunoprecipitation (ChIP) assays directed to two HREs identified in the proximal promoters of CKB for either PyMT cells or MCF7 cells revealed enrichment for HIF-1α for at least one HRE site.

CKB mRNA and protein levels were decreased in PyMT HIF-1 WT and KO end-stage tumors. However, this difference was not as dramatic as was observed in cultured tumor epithelial cells. A significant difference in *Ckb* mRNA expression in tumors by qPCR was observed only after raw data were normalized to the epithelial cell marker, keratin 8 (*Krt18*). It is highly likely that since HIF-1 loss, and therefore, decreased CKB, is only targeted to the tumor epithelium, a significant proportion of the CKB signal observed in whole tumor extracts by western blotting

is derived from the mammary stroma. In particular, CKB is expressed in adipose, macrophages, and endothelial cells [47, 92-94].

Knockdown of *Ckb* in PyMT cells via shRNA significantly reduced total creatine kinase enzymatic activity but produced only minor changes in cell proliferation *in vitro*, and no differences in wound healing/cell migration. The biological activities predominantly impacted in response to *Ckb* shRNA KD were the repression of invasion through extracellular matrix (ECM), particularly at hypoxia, and the reduction of intracellular ATP levels. These results suggested that when ATP levels are limited and tumor cells are primarily relying on glycolysis, the creatine kinase arm of metabolism becomes essential to produce the energy necessary for cell invasion. Consistent with prior studies in ovarian cancer cells that CKB loss of function represses glycolysis [72], Seahorse analysis revealed that *Ckb* KD reduced maximal glycolytic activity, and in sh61 KD cells, also reduced glycolytic capacity. Surprisingly, in sh61 KD cells, basal respiration and maximum respiration (oxidative phosphorylation outputs) were also impaired, and there was a reduction in ATP levels observed for both *Ckb* KD pools. Although it has been proposed that cytosolic CK isoforms interface with the mitochondrial CK isoforms to maintain energy flux [25], recently, in thermogenic brown fat, CKB protein was found to directly shuttle between mitochondria and the cytoplasm, directly regulating mitochondrial ATP turnover [94]. Nevertheless, deletion of the CKB isoform impaired energy production through both glycolysis and mitochondrial respiration in the presence of atmospheric oxygen.

In contrast to our expectations based on the minimal changes in cellular proliferation in response to the loss of CKB, there was a robust and significant decrease in tumor growth when PyMT *Ckb* KD cultured cells were implanted into the wild type mammary fat pad *in vivo*. Remarkably, deletion of a single HIF-1 target gene, *Ckb*, produced tumor volumes highly similar to those of HIF-1α KO cells. These results suggest that, *in vivo*, tumor cell-intrinsic CKB directly influences the local surrounding microenvironment to promote tumorigenesis, and that defects in epithelial-derived CKB disrupt a paracrine network necessary to promote tumor growth. For example, local extracellular secretion of CKB by colon cancer cells into the liver microenvironment was shown to promote metastatic outgrowth through the extracellular production of phosphocreatine (PCr) that was then utilized by tumor cells as an energy source [44].

Because overall survival (measured as morbidity due to lung metastasis) increases when *Ckb* is knocked out in the PyMT tumor epithelium and the primary tumors are resected to stimulate lung metastasis, it is clear that CKB is necessary for efficient completion of the entire metastatic cascade. The on-target specificity and the favorable safety profile of cyclocreatine (cCr) [66] make this small molecule inhibitor an excellent pre-clinical tool to ascertain the effects of loss of CKB activity upon the formation of metastases to complement genetic manipulation approaches. To confirm the relevance of CKB expression to late-stage metastasis, tail vein assays were also used, revealing a significant decrease in colonization to the lung, either by knocking down *Ckb* or by inhibiting total CK activity with cCr therapy. Blocking CK activity by daily systemic treatment with cCr of mice bearing

PyMT tumor cells resulted in a significant decrease in the ability of cells to colonize the lungs and to form lung macro-metastases. Additionally, conversion of pre-established micro-metastases to macro-metastases was also blocked by cCr treatment, as was demonstrated by delaying cCr therapy until 7 days after cells were injected into mice. Additional studies are warranted to ascertain exactly how HIF-1α-dependent modulation of CKB expression contributes to each step of the metastatic cascade. Whether cCr monotherapy blocks primary tumor growth was not tested. Of interest, recent studies in a liver cancer model (HCT116) and in the 4T1 TNBC-like model [95], creatine supplementation, which increases creatine kinase flux, was not sufficient to change primary tumor growth rate, but significantly promoted lung metastasis in mice bearing 4T1 cells.

It is likely that, in addition to lung colonization and the conversion of lung micro-metastases to macro-metastases, the early stages of tumor cell invasion are directly modulated through CKB. This conclusion is based on our observations that deletion of CKB in PyMT cells impairs invasion through Matrigel whereas the over-expression of CKB in MDA-MB-231 cells enhances not only chemotaxis and cell invasion, but also promotes invadopodia activity. The apparent relationship between a master regulator of cellular metabolism, such as HIF-1, and its target CKB, and the degradation of extracellular matrix by invadopodia is intriguing. In a proteomics screen to identify factors enriched in invadopodia, multiple, HIF-dependent metabolic enzymes were identified, including GAPDH, enolase 1, lactate dehydrogenase (LDH), pyruvate kinase, muscle 2 (PKM2), and phosphoglycerate kinase 1 (PGK1) [62].

In 2009, it was proposed that local ATP generation coordinated by CKB facilitates cell motility in astrocytes and fibroblasts [47]. The direct relationship of creatine flux to ATP levels and to cell motility was recently validated in detail using pancreatic cancer models [45]. Notably, this same study also revealed that CKB, but not other CK isoforms, is a Yes-associated protein (YAP)-responsive mechanosensory responder [45]. In particular, YAP increases CKB expression and CK activity in response to a stiff extracellular environment (such as glass). Of interest, *in vivo*, increased expression of YAP was found to promote breast tumorigenesis, although it appeared to be dispensable for normal mammary gland development [96]. These connections between YAP and HIF and CKB are of interest since YAP can induce HIF-1α [96] through mechanical loading [97], and since hypoxia/HIF-1 can also stimulate also YAP activity through 14-3-3-zeta [98], potentially setting up feed-forward loops necessary for metastatic potential in solid tumors that are executed via CKB.

In multiple TNBC cell lines, we found that pairing cCr with conventional chemotherapies (Taxol and doxorubicin) enhanced cCr efficacy, with either additive or synergistic effects, depending on the cell line model and cytotoxic agent. In MCF-7 cells, cCr was previously shown to stabilize microtubule networks within 24 h of treatment and appeared to preferentially target new microtubules rather than established networks [81]. Combining cCr with Taxol was reported to be synergistic in reducing the fraction of cells surviving treatment, although formal isobole testing was not utilized in this report. We observed the most potent inhibition of cell growth in TNBC models when cCr was paired with Taxol. In

addition, cCr treatment was synergistic with DOX near the IC_{50} of DOX in two TNBC cell lines (MDA-MB-468 and MDA-MB-453) but was antagonistic with cCr in BT549 cells. It has been shown that doxorubicin treatment can impact heart microtubule structure by impairing reassembly [99]. However, the exact mechanisms of DOX synergy remain undefined. Overall, we conclude that cCr interferes with cell growth, inhibits cell cycle progression, and impairs chemotaxis/cell invasion likely through both its effects on cellular metabolism as well as microtubule dynamics. Of note, YAP expression has also been shown to correlate with HIF-dependent adriamycin (DOX) resistance in leukemia [100]. And, down-regulation of CKB in Skov3 ovarian cancer cells enhanced sensitivity to doxorubicin [72]. Whether the YAP-dependent mechano-sensing potential of CKB is involved in chemotherapy sensitivity remains to be tested.

We propose that creatine kinase inhibition is a promising clinical intervention, particularly for patients with metastatic disease. cCr likely crosses the blood-brain barrier and is known to function as a phosphagen in the brain [40, 101, 102], suggesting that creatine analogs may be useful to target brain metastases, as well as lung and visceral metastases. Systemic cCr therapy is well-tolerated in rodents and ameliorates defects in cognitive behavior in mice deficient for the creatine transporter (*Slc6a8*) [41], consistent with prior observations that creatine kinase activity and CKB expression in the brain are necessary for learning [27]. In addition, deletion of *CKB* or the systemic administration of cCr is protective against bone loss in mice subjected to either ovariectomy or lipopolysaccharide (LPS)

challenge [103], suggesting potential clinical applications to ameliorate osteolytic destruction of bone, the most common site of metastasis in breast cancer patients.

In limited clinical trials to date, cyclocreatine was well-tolerated [25]. A new generation derivative of cCr known as LUM-001 with enhanced bio-availability (Lumos Pharmaceuticals) was developed to treat creatine transporter deficiency (CTD). LUM-001 has also been tested in rodents to treat neurodevelopmental cognitive disorders, including autism [40]. Clinical trials using LUM-001 are currently in enrollment (www.clinicaltrials.gov; NCT02931682) after pre-clinical studies were conducted with support from the NIH Therapeutics for Rare and Neglected Diseases (TRND) program [104], which generated the pre-clinical data to support an Investigational New Drug (IND) application to the FDA.

Overall, our results demonstrate that CKB is a major effector of HIF-1-mediated promotion of breast tumorigenesis and lung metastasis in ER-negative breast cancer *in vitro* and *in vivo*, capable of eliciting aggressive phenotypes in the context of normoxia or hypoxia. Co-targeting multiple downstream HIF targets, such as CKB and VEGF, as part of a combinatorial breast cancer treatment strategy, may more effectively disrupt HIF-driven processes that drive the metastatic cascade. A growing body of evidence indicates that cCr has efficacy in a wide variety of breast cancer subtypes, including HER2+ and ER+ positive breast cancer, and as reported herein, in ER-negative/basal breast cancer models. New clinical trials to explore cCr monotherapy versus combination with either Taxol or doxorubicin would be predicted to demonstrate prolonged survival through reduced shedding of cancer cells into the circulation, and/or by impairing the

growth of tumor cells already disseminated to distant organs, including brain and bone metastases.

References Cited

1. **Cancer Stat Facts: Female Breast Cancer** [https://seer.cancer.gov/statfacts/html/breast.html]
2. Marquette C, Nabell L: **Chemotherapy-resistant metastatic breast cancer**. *Curr Treat Options Oncol* 2012, **13**(2):263-275.
3. Bailey KM, Wojtkowiak JW, Hashim AI, Gillies RJ: **Targeting the metabolic microenvironment of tumors**. *Adv Pharmacol* 2012, **65**:63-107.
4. Zhao Y, Butler EB, Tan M: **Targeting cellular metabolism to improve cancer therapeutics**. *Cell Death Dis* 2013, **4**:e532.
5. Dang NH, Singla AK, Mackay EM, Jirik FR, Weljie AM: **Targeted Cancer Therapeutics: Biosynthetic and Energetic Pathways Characterized by Metabolomics and the Interplay with Key Cancer Regulatory Factors**. *Curr Pharm Des* 2013.
6. Semenza GL: **HIF-1 mediates metabolic responses to intratumoral hypoxia and oncogenic mutations**. *J Clin Invest* 2013, **123**(9):3664-3671.
7. Tormos KV, Chandel NS: **Inter-connection between mitochondria and HIFs**. *J Cell Mol Med* 2010, **14**(4):795-804.
8. Chiche J, Brahimi-Horn MC, Pouyssegur J: **Tumour hypoxia induces a metabolic shift causing acidosis: a common feature in cancer**. *J Cell Mol Med* 2010, **14**(4):771-794.
9. Rohwer N, Cramer T: **Hypoxia-mediated drug resistance: novel insights on the functional interaction of HIFs and cell death pathways**. *Drug Resist Updat* 2011, **14**(3):191-201.
10. Brown JM: **Exploiting the hypoxic cancer cell: mechanisms and therapeutic strategies**. *Mol Med Today* 2000, **6**(4):157-162.
11. Gupta GP, Massague J: **Cancer metastasis: building a framework**. *Cell* 2006, **127**(4):679-695.
12. Liao D, Corle C, Seagroves TN, Johnson RS: **Hypoxia-inducible factor-1alpha is a key regulator of metastasis in a transgenic model of cancer initiation and progression**. *Cancer Res* 2007, **67**(2):563-572.
13. Schwab LP, Peacock DL, Majumdar D, Ingels JF, Jensen LC, Smith KD, Cushing RC, Seagroves TN: **Hypoxia-inducible factor 1alpha promotes primary tumor growth and tumor-initiating cell activity in breast cancer**. *Breast Cancer Res* 2012, **14**(1):R6.
14. Chi JT, Wang Z, Nuyten DS, Rodriguez EH, Schaner ME, Salim A, Wang Y, Kristensen GB, Helland A, Borresen-Dale AL *et al*: **Gene expression programs in response to hypoxia: cell type specificity and prognostic significance in human cancers**. *PLoS Med* 2006, **3**(3):e47.
15. Dales JP, Garcia S, Meunier-Carpentier S, Andrac-Meyer L, Haddad O, Lavaut MN, Allasia C, Bonnier P, Charpin C: **Overexpression of hypoxia-inducible factor HIF-1alpha predicts early relapse in breast cancer: retrospective study in a series of 745 patients**. *Int J Cancer* 2005, **116**(5):734-739.
16. Gruber G, Greiner RH, Hlushchuk R, Aebersold DM, Altermatt HJ, Berclaz G, Djonov V: **Hypoxia-inducible factor 1 alpha in high-risk breast**

cancer: an independent prognostic parameter? *Breast Cancer Res* 2004, **6**(3):R191-198.
17. Hunter K, Welch DR, Liu ET: **Genetic background is an important determinant of metastatic potential**. *Nature genetics* 2003, **34**(1):23-24; author reply 25.
18. Xia Y, Choi HK, Lee K: **Recent advances in hypoxia-inducible factor (HIF)-1 inhibitors**. *Eur J Med Chem* 2012, **49**:24-40.
19. Chen W, Hill H, Christie A, Kim MS, Holloman E, Pavia-Jimenez A, Homayoun F, Ma Y, Patel N, Yell P *et al*: **Targeting renal cell carcinoma with a HIF-2 antagonist**. *Nature* 2016, **539**(7627):112-117.
20. Courtney KD, Ma Y, Diaz de Leon A, Christie A, Xie Z, Woolford L, Singla N, Joyce A, Hill H, Madhuranthakam AJ *et al*: **HIF-2 Complex Dissociation, Target Inhibition, and Acquired Resistance with PT2385, a First-in-Class HIF-2 Inhibitor, in Patients with Clear Cell Renal Cell Carcinoma**. *Clin Cancer Res* 2020, **26**(4):793-803.
21. Doedens A, Johnson RS: **Transgenic models to understand hypoxia-inducible factor function**. *Methods Enzymol* 2007, **435**:87-105.
22. Keith B, Johnson RS, Simon MC: **HIF1alpha and HIF2alpha: sibling rivalry in hypoxic tumour growth and progression**. *Nat Rev Cancer* 2012, **12**(1):9-22.
23. Wallimann T, Wyss M, Brdiczka D, Nicolay K, Eppenberger HM: **Intracellular compartmentation, structure and function of creatine kinase isoenzymes in tissues with high and fluctuating energy demands: the 'phosphocreatine circuit' for cellular energy homeostasis**. *Biochem J* 1992, **281 (Pt 1)**:21-40.
24. Wallimann T, Tokarska-Schlattner M, Schlattner U: **The creatine kinase system and pleiotropic effects of creatine**. *Amino Acids* 2011, **40**(5):1271-1296.
25. Wyss M, Kaddurah-Daouk R: **Creatine and creatinine metabolism**. *Physiol Rev* 2000, **80**(3):1107-1213.
26. Glover LE, Bowers BE, Saeedi B, Ehrentraut SF, Campbell EL, Bayless AJ, Dobrinskikh E, Kendrick AA, Kelly CJ, Burgess A *et al*: **Control of creatine metabolism by HIF is an endogenous mechanism of barrier regulation in colitis**. *Proc Natl Acad Sci U S A* 2013, **110**(49):19820-19825.
27. Jost CR, Van Der Zee CE, In 't Zandt HJ, Oerlemans F, Verheij M, Streijger F, Fransen J, Heerschap A, Cools AR, Wieringa B: **Creatine kinase B-driven energy transfer in the brain is important for habituation and spatial learning behaviour, mossy fibre field size and determination of seizure susceptibility**. *Eur J Neurosci* 2002, **15**(10):1692-1706.
28. Streijger F, Oerlemans F, Ellenbroek BA, Jost CR, Wieringa B, Van der Zee CE: **Structural and behavioural consequences of double deficiency for creatine kinases BCK and UbCKmit**. *Behav Brain Res* 2005, **157**(2):219-234.
29. Hornemann T, Rutishauser D, Wallimann T: **Why is creatine kinase a dimer? Evidence for cooperativity between the two subunits**. *Biochim Biophys Acta* 2000, **1480**(1-2):365-373.

30. Balasubramani M, Day BW, Schoen RE, Getzenberg RH: **Altered expression and localization of creatine kinase B, heterogeneous nuclear ribonucleoprotein F, and high mobility group box 1 protein in the nuclear matrix associated with colon cancer**. *Cancer Res* 2006, **66**(2):763-769.
31. Harty MW, Huddleston HM, Papa EF, Puthawala T, Tracy AP, Ramm GA, Gehring S, Gregory SH, Tracy TF, Jr.: **Repair after cholestatic liver injury correlates with neutrophil infiltration and matrix metalloproteinase 8 activity**. *Surgery* 2005, **138**(2):313-320.
32. Hemmer W, Zanolla E, Furter-Graves EM, Eppenberger HM, Wallimann T: **Creatine kinase isoenzymes in chicken cerebellum: specific localization of brain-type creatine kinase in Bergmann glial cells and muscle-type creatine kinase in Purkinje neurons**. *Eur J Neurosci* 1994, **6**(4):538-549.
33. Mooney SM, Rajagopalan K, Williams BH, Zeng Y, Christudass CS, Li Y, Yin B, Kulkarni P, Getzenberg RH: **Creatine kinase brain overexpression protects colorectal cells from various metabolic and non-metabolic stresses**. *J Cell Biochem* 2011, **112**(4):1066-1075.
34. Zarghami N, Giai M, Yu H, Roagna R, Ponzone R, Katsaros D, Sismondi P, Diamandis EP: **Creatine kinase BB isoenzyme levels in tumour cytosols and survival of breast cancer patients**. *Br J Cancer* 1996, **73**(3):386-390.
35. Chen H, Pimienta G, Gu Y, Sun X, Hu J, Kim MS, Chaerkady R, Gucek M, Cole RN, Sukumar S *et al*: **Proteomic characterization of Her2/neu-overexpressing breast cancer cells**. *Proteomics* 2010, **10**(21):3800-3810.
36. Chen WZ, Pang B, Yang B, Zhou JG, Sun YH: **Differential proteome analysis of conditioned medium of BPH-1 and LNCaP cells**. *Chin Med J (Engl)* 2011, **124**(22):3806-3809.
37. Xu Y, Cao LQ, Jin LY, Chen ZC, Zeng GQ, Tang CE, Li GQ, Duan CJ, Peng F, Xiao ZQ *et al*: **Quantitative proteomic study of human lung squamous carcinoma and normal bronchial epithelial acquired by laser capture microdissection**. *J Biomed Biotechnol* 2012, **2012**:510418.
38. Zeng GQ, Zhang PF, Deng X, Yu FL, Li C, Xu Y, Yi H, Li MY, Hu R, Zuo JH *et al*: **Identification of candidate biomarkers for early detection of human lung squamous cell cancer by quantitative proteomics**. *Mol Cell Proteomics* 2012, **11**(6):M111 013946.
39. Kurmi K, Hitosugi S, Yu J, Boakye-Agyeman F, Wiese EK, Larson TR, Dai Q, Machida YJ, Lou Z, Wang L *et al*: **Tyrosine Phosphorylation of Mitochondrial Creatine Kinase 1 Enhances a Druggable Tumor Energy Shuttle Pathway**. *Cell Metab* 2018, **28**(6):833-847 e838.
40. Cacciante F, Gennaro M, Sagona G, Mazziotti R, Lupori L, Cerri E, Putignano E, Butt M, Do MT, McKew JC *et al*: **Cyclocreatine treatment ameliorates the cognitive, autistic and epileptic phenotype in a mouse model of Creatine Transporter Deficiency**. *Sci Rep* 2020, **10**(1):18361.

41. Kurosawa Y, Degrauw TJ, Lindquist DM, Blanco VM, Pyne-Geithman GJ, Daikoku T, Chambers JB, Benoit SC, Clark JF: **Cyclocreatine treatment improves cognition in mice with creatine transporter deficiency**. *J Clin Invest* 2012, **122**(8):2837-2846.
42. Teicher BA, Menon K, Northey D, Liu J, Kufe DW, Kaddurah-Daouk R: **Cyclocreatine in cancer chemotherapy**. *Cancer Chemother Pharmacol* 1995, **35**(5):411-416.
43. Mulvaney PT, Stracke ML, Nam SW, Woodhouse E, O'Keefe M, Clair T, Liotta LA, Khaddurah-Daouk R, Schiffmann E: **Cyclocreatine inhibits stimulated motility in tumor cells possessing creatine kinase**. *Int J Cancer* 1998, **78**(1):46-52.
44. Loo JM, Scherl A, Nguyen A, Man FY, Weinberg E, Zeng Z, Saltz L, Paty PB, Tavazoie SF: **Extracellular metabolic energetics can promote cancer progression**. *Cell* 2015, **160**(3):393-406.
45. Papalazarou V, Zhang T, Paul NR, Juin A, Cantini M, Maddocks ODK, Salmeron-Sanchez M, Machesky LM: **The creatine-phosphagen system is mechanoresponsive in pancreatic adenocarcinoma and fuels invasion and metastasis**. *Nat Metab* 2020, **2**(1):62-80.
46. Kuiper JW, Pluk H, Oerlemans F, van Leeuwen FN, de Lange F, Fransen J, Wieringa B: **Creatine kinase-mediated ATP supply fuels actin-based events in phagocytosis**. *PLoS Biol* 2008, **6**(3):e51.
47. Kuiper JW, van Horssen R, Oerlemans F, Peters W, van Dommelen MM, te Lindert MM, ten Hagen TL, Janssen E, Fransen JA, Wieringa B: **Local ATP generation by brain-type creatine kinase (CK-B) facilitates cell motility**. *PLoS One* 2009, **4**(3):e5030.
48. van Horssen R, Janssen E, Peters W, van de Pasch L, Lindert MM, van Dommelen MM, Linssen PC, Hagen TL, Fransen JA, Wieringa B: **Modulation of cell motility by spatial repositioning of enzymatic ATP/ADP exchange capacity**. *J Biol Chem* 2009, **284**(3):1620-1627.
49. Dent R, Hanna WM, Trudeau M, Rawlinson E, Sun P, Narod SA: **Pattern of metastatic spread in triple-negative breast cancer**. *Breast Cancer Res Treat* 2009, **115**(2):423-428.
50. Kennecke H, Yerushalmi R, Woods R, Cheang MC, Voduc D, Speers CH, Nielsen TO, Gelmon K: **Metastatic behavior of breast cancer subtypes**. *J Clin Oncol* 2010, **28**(20):3271-3277.
51. Wu Q, Li J, Zhu S, Wu J, Chen C, Liu Q, Wei W, Zhang Y, Sun S: **Breast cancer subtypes predict the preferential site of distant metastases: a SEER based study**. *Oncotarget* 2017, **8**(17):27990-27996.
52. Shamir R, Maron-Katz A, Tanay A, Linhart C, Steinfeld I, Sharan R, Shiloh Y, Elkon R: **EXPANDER--an integrative program suite for microarray data analysis**. *BMC Bioinformatics* 2005, **6**:232.
53. Network CGA: **Comprehensive molecular portraits of human breast tumours**. *Nature* 2012, **490**(7418):61-70.
54. Nagy A, Lanczky A, Menyhart O, Gyorffy B: **Validation of miRNA prognostic power in hepatocellular carcinoma using expression data of independent datasets**. *Sci Rep* 2018, **8**(1):9227.

55. Brooks DL, Schwab LP, Krutilina R, Parke DN, Sethuraman A, Hoogewijs D, Schorg A, Gotwald L, Fan M, Wenger RH *et al*: **ITGA6 is directly regulated by hypoxia-inducible factors and enriches for cancer stem cell activity and invasion in metastatic breast cancer models**. *Mol Cancer* 2016, **15**:26.
56. Brooks DL, Seagroves TN: **Chromatin Immunoprecipitation of HIF-alpha in Breast Tumor Cells Using Wild Type and Loss of Function Models**. *Methods Mol Biol* 2018, **1742**:67-79.
57. Oosthuyse B, Moons L, Storkebaum E, Beck H, Nuyens D, Brusselmans K, Van Dorpe J, Hellings P, Gorselink M, Heymans S *et al*: **Deletion of the hypoxia-response element in the vascular endothelial growth factor promoter causes motor neuron degeneration**. *Nature genetics* 2001, **28**(2):131-138.
58. Choi BH, Ha Y, Ahn CH, Huang X, Kim JM, Park SR, Park H, Park HC, Kim SW, Lee M: **A hypoxia-inducible gene expression system using erythropoietin 3' untranslated region for the gene therapy of rat spinal cord injury**. *Neurosci Lett* 2007, **412**(2):118-122.
59. Martin KH, Hayes KE, Walk EL, Ammer AG, Markwell SM, Weed SA: **Quantitative measurement of invadopodia-mediated extracellular matrix proteolysis in single and multicellular contexts**. *J Vis Exp* 2012(66):e4119.
60. Tallarida RJ: **An overview of drug combination analysis with isobolograms**. *J Pharmacol Exp Ther* 2006, **319**(1):1-7.
61. Appelhoff RJ, Tian YM, Raval RR, Turley H, Harris AL, Pugh CW, Ratcliffe PJ, Gleadle JM: **Differential function of the prolyl hydroxylases PHD1, PHD2, and PHD3 in the regulation of hypoxia-inducible factor**. *J Biol Chem* 2004, **279**(37):38458-38465.
62. Attanasio F, Caldieri G, Giacchetti G, van Horssen R, Wieringa B, Buccione R: **Novel invadopodia components revealed by differential proteomic analysis**. *Eur J Cell Biol* 2011, **90**(2-3):115-127.
63. Matsumoto K, Arao T, Tanaka K, Kaneda H, Kudo K, Fujita Y, Tamura D, Aomatsu K, Tamura T, Yamada Y *et al*: **mTOR signal and hypoxia-inducible factor-1 alpha regulate CD133 expression in cancer cells**. *Cancer research* 2009, **69**(18):7160-7164.
64. Wong CC, Gilkes DM, Zhang H, Chen J, Wei H, Chaturvedi P, Fraley SI, Wong CM, Khoo US, Ng IO *et al*: **Hypoxia-inducible factor 1 is a master regulator of breast cancer metastatic niche formation**. *Proc Natl Acad Sci U S A* 2011, **108**(39):16369-16374.
65. Annesley TM, Walker JB: **Cyclocreatine phosphate as a substitute for creatine phosphate in vertebrate tissues. Energistic considerations**. *Biochem Biophys Res Commun* 1977, **74**(1):185-190.
66. Bergnes G, Yuan W, Khandekar VS, O'Keefe MM, Martin KJ, Teicher BA, Kaddurah-Daouk R: **Creatine and phosphocreatine analogs: anticancer activity and enzymatic analysis**. *Oncol Res* 1996, **8**(3):121-130.
67. Hunter KW, Broman KW, Voyer TL, Lukes L, Cozma D, Debies MT, Rouse J, Welch DR: **Predisposition to efficient mammary tumor metastatic**

progression is linked to the breast cancer metastasis suppressor gene Brms1. *Cancer Res* 2001, **61**(24):8866-8872.
68. Wang F, Samudio I, Safe S: **Transcriptional activation of rat creatine kinase B by 17beta-estradiol in MCF-7 cells involves an estrogen responsive element and GC-rich sites**. *J Cell Biochem* 2001, **84**(1):156-172.
69. Stiehl DP, Bordoli MR, Abreu-Rodriguez I, Wollenick K, Schraml P, Gradin K, Poellinger L, Kristiansen G, Wenger RH: **Non-canonical HIF-2alpha function drives autonomous breast cancer cell growth via an AREG-EGFR/ErbB4 autocrine loop**. *Oncogene* 2012, **31**(18):2283-2297.
70. Lillie JW, O'Keefe M, Valinski H, Hamlin HA, Jr., Varban ML, Kaddurah-Daouk R: **Cyclocreatine (1-carboxymethyl-2-iminoimidazolidine) inhibits growth of a broad spectrum of cancer cells derived from solid tumors**. *Cancer Res* 1993, **53**(13):3172-3178.
71. Martin K, Winslow E, Okeefe M, Khandekar V, Hamlin A, Lillie J, Kaddurahdaouk R: **Specific targeting of tumor cells by the creatine analog cyclocreatine**. *Int J Oncol* 1996, **9**(5):993-999.
72. Li XH, Chen XJ, Ou WB, Zhang Q, Lv ZR, Zhan Y, Ma L, Huang T, Yan YB, Zhou HM: **Knockdown of creatine kinase B inhibits ovarian cancer progression by decreasing glycolysis**. *Int J Biochem Cell Biol* 2013, **45**(5):979-986.
73. Martin KJ, Winslow ER, Kaddurah-Daouk R: **Cell cycle studies of cyclocreatine, a new anticancer agent**. *Cancer Res* 1994, **54**(19):5160-5165.
74. Hoosein NM, Martin KJ, Abdul M, Logothetis CJ, Kaddurah-Daouk R: **Antiproliferative effects of cyclocreatine on human prostatic carcinoma cells**. *Anticancer Res* 1995, **15**(4):1339-1342.
75. Miller EE, Evans AE, Cohn M: **Inhibition of rate of tumor growth by creatine and cyclocreatine**. *Proc Natl Acad Sci U S A* 1993, **90**(8):3304-3308.
76. Fenouille N, Bassil CF, Ben-Sahra I, Benajiba L, Alexe G, Ramos A, Pikman Y, Conway AS, Burgess MR, Li Q *et al*: **The creatine kinase pathway is a metabolic vulnerability in EVI1-positive acute myeloid leukemia**. *Nat Med* 2017, **23**(3):301-313.
77. Lehmann BD, Bauer JA, Chen X, Sanders ME, Chakravarthy AB, Shyr Y, Pietenpol JA: **Identification of human triple-negative breast cancer subtypes and preclinical models for selection of targeted therapies**. *J Clin Invest* 2011, **121**(7):2750-2767.
78. Lawrence RT, Perez EM, Hernandez D, Miller CP, Haas KM, Irie HY, Lee SI, Blau CA, Villen J: **The Proteomic Landscape of Triple-Negative Breast Cancer**. *Cell Rep* 2015, **11**(6):990.
79. Vranic S, Gatalica Z, Wang ZY: **Update on the molecular profile of the MDA-MB-453 cell line as a model for apocrine breast carcinoma studies**. *Oncol Lett* 2011, **2**(6):1131-1137.
80. Chevalier C, Cannet A, Descamps S, Sirvent A, Simon V, Roche S, Benistant C: **ABL tyrosine kinase inhibition variable effects on the**

invasive properties of different triple negative breast cancer cell lines. *PLoS One* 2015, **10**(3):e0118854.

81. Martin KJ, Vassallo CD, Teicher BA, Kaddurah-Daouk R: **Microtubule stabilization and potentiation of taxol activity by the creatine analog cyclocreatine**. *Anticancer Drugs* 1995, **6**(3):419-426.
82. Bos R, van Diest PJ, de Jong JS, van der Groep P, van der Valk P, van der Wall E: **Hypoxia-inducible factor-1alpha is associated with angiogenesis, and expression of bFGF, PDGF-BB, and EGFR in invasive breast cancer**. *Histopathology* 2005, **46**(1):31-36.
83. Chaturvedi P, Gilkes DM, Wong CC, Kshitiz, Luo W, Zhang H, Wei H, Takano N, Schito L, Levchenko A *et al*: **Hypoxia-inducible factor-dependent breast cancer-mesenchymal stem cell bidirectional signaling promotes metastasis**. *J Clin Invest* 2013, **123**(1):189-205.
84. Chen J, Imanaka N, Griffin JD: **Hypoxia potentiates Notch signaling in breast cancer leading to decreased E-cadherin expression and increased cell migration and invasion**. *Br J Cancer* 2010, **102**(2):351-360.
85. Goonewardene TI, Sowter HM, Harris AL: **Hypoxia-induced pathways in breast cancer**. *Microsc Res Tech* 2002, **59**(1):41-48.
86. Gort EH, Groot AJ, Derks van de Ven TL, van der Groep P, Verlaan I, van Laar T, van Diest PJ, van der Wall E, Shvarts A: **Hypoxia-inducible factor-1alpha expression requires PI 3-kinase activity and correlates with Akt1 phosphorylation in invasive breast carcinomas**. *Oncogene* 2006, **25**(45):6123-6127.
87. Krishnamachary B, Semenza GL: **Analysis of hypoxia-inducible factor 1alpha expression and its effects on invasion and metastasis**. *Methods Enzymol* 2007, **435**:347-354.
88. Gatza ML, Kung HN, Blackwell KL, Dewhirst MW, Marks JR, Chi JT: **Analysis of tumor environmental response and oncogenic pathway activation identifies distinct basal and luminal features in HER2-related breast tumor subtypes**. *Breast Cancer Res* 2011, **13**(3):R62.
89. Bos R, Zhong H, Hanrahan CF, Mommers E, Semenza GL, Pinedo HM, Abeloff MD, Simons JW, van Diest PJ, van der Wall E: **Levels of hypoxia-inducible factor-1a during breast carcinogenesis**. *J Natl Cancer Instit* 2001, **93**(4):309-314.
90. Lee JW, Bae SH, Jeong JW, Kim SH, Kim KW: **Hypoxia-inducible factor (HIF-1)alpha: its protein stability and biological functions**. *Exp Mol Med* 2004, **36**(1):1-12.
91. Semenza GL: **Targeting HIF-1 for cancer therapy**. *Nat Rev Cancer* 2003, **3**(10):721-732.
92. Decking UK, Alves C, Wallimann T, Wyss M, Schrader J: **Functional aspects of creatine kinase isoenzymes in endothelial cells**. *Am J Physiol Cell Physiol* 2001, **281**(1):C320-328.
93. Loike JD, Kozler VF, Silverstein SC: **Creatine kinase expression and creatine phosphate accumulation are developmentally regulated**

during differentiation of mouse and human monocytes. *J Exp Med* 1984, **159**(3):746-757.
94. Rahbani JF, Roesler A, Hussain MF, Samborska B, Dykstra CB, Tsai L, Jedrychowski MP, Vergnes L, Reue K, Spiegelman BM *et al*: **Creatine kinase B controls futile creatine cycling in thermogenic fat**. *Nature* 2021, **590**(7846):480-485.
95. Zhang L, Zhu Z, Yan H, Wang W, Wu Z, Zhang F, Zhang Q, Shi G, Du J, Cai H *et al*: **Creatine promotes cancer metastasis through activation of Smad2/3**. *Cell Metab* 2021, **33**(6):1111-1123 e1114.
96. Chen Q, Zhang N, Gray RS, Li H, Ewald AJ, Zahnow CA, Pan D: **A temporal requirement for Hippo signaling in mammary gland differentiation, growth, and tumorigenesis**. *Genes Dev* 2014, **28**(5):432-437.
97. Jing X, Yang X, Zhang W, Wang S, Cui X, Du T, Li T: **Mechanical loading induces HIF-1alpha expression in chondrocytes via YAP**. *Biotechnol Lett* 2020, **42**(9):1645-1654.
98. Jia Y, Li HY, Wang J, Wang Y, Zhang P, Ma N, Mo SJ: **Phosphorylation of 14-3-3zeta links YAP transcriptional activation to hypoxic glycolysis for tumorigenesis**. *Oncogenesis* 2019, **8**(5):31.
99. Rabkin SW, Sunga P: **The effect of doxorubicin (adriamycin) on cytoplasmic microtubule system in cardiac cells**. *J Mol Cell Cardiol* 1987, **19**(11):1073-1083.
100. Zhu B, Pan S, Liu J, Wang S, Ni Y, Xiao L, Wei Q, Peng Y, Ding Z, Zhao W: **HIF-1alpha forms regulatory loop with YAP to coordinate hypoxia-induced adriamycin resistance in acute myeloid leukemia cells**. *Cell Biol Int* 2020, **44**(2):456-466.
101. Uemura T, Ito S, Masuda T, Shimbo H, Goto T, Osaka H, Wada T, Couraud PO, Ohtsuki S: **Cyclocreatine Transport by SLC6A8, the Creatine Transporter, in HEK293 Cells, a Human Blood-Brain Barrier Model Cell, and CCDSs Patient-Derived Fibroblasts**. *Pharm Res* 2020, **37**(3):61.
102. Woznicki DT, Walker JB: **Formation of a supplemental long time-constant reservoir of high energy phosphate by brain in vivo and in vitro and its reversible depletion by potassium depolarization**. *J Neurochem* 1979, **33**(1):75-80.
103. Chang EJ, Ha J, Oerlemans F, Lee YJ, Lee SW, Ryu J, Kim HJ, Lee Y, Kim HM, Choi JY *et al*: **Brain-type creatine kinase has a crucial role in osteoclast-mediated bone resorption**. *Nat Med* 2008, **14**(9):966-972.
104. **LUM-001 as a treatment for creatine transporter deficiency** [https://ncats.nih.gov/trnd/projects/complete/cincy-creatine-transporter-defect]

Acknowledgments. We are grateful to the staff of the institutional core facilities at The University of Tennessee Health Science Center, who supported this work, including Dr. William Taylor and Mr. Lorne Rose of the Molecular Resource Center of Excellence (MRC) for providing microarray support. Dr. Deidre Daria assisted with cell cycle analysis at the Flow Cytometry and Cell Sorting Core (FCCS), and Dr. Daniel Johnson provided optimized data analysis workflows and long-term data storage at the Molecular Bioinformatics (mBIO) core. All paraffin-embedded tissue sections were prepared in the UTHSC Research Histology Core (RHC) in partnership with the Department of Pathology with support from the laboratory manager LaShawn Barnett. We thank the Department of Pathology and the Center for Cancer Research at UTHSC for support to digitally scan all immunostained slides and for providing access to the 3D Histech software analysis workstation to quantitate immunostaining patterns. The UTHSC Department of Pediatrics supports the Seahorse XF instrument managed by Dr. Heather Smallwood. We thank Dr. Athena Starland-Davenport and Dr. Rob Williams of the UTHSC Department of Genetics, Genomics, and Informatics for providing access to the Nikon ECLIPSE Ti2 microscope. The UTHSC Center for Cancer Research provided and supported the IncuCyte S3 live-cell imager shared instrumentation. Elizabeth Cox and her team at the University of Arizona Genetics Core provided cell line authentication (via the Science Exchange network). This work was supported by NIH grant R01 CA138488 (to T.N. Seagroves), the Department of Defense Breast Cancer Research Program (BC150640 to T.N. Seagroves), the METAvivor foundation (to T.N. Seagroves), and an internal investigator bridge

funding program from the UTHSC Office of Research. D. Layman was supported by a summer fellowship from the West Cancer Center (Memphis, TN) and D. Oluwalana, a graduate student in the UTHSC College of Graduate Health Sciences, was supported through the Department of Pathology.

Author disclosures. R.I. Krutilina, **H.C. Playa**, **D.L Brooks**, **L.P. Schwab,** and **D.N. Parke** report grant support from the CDMRP/Department of Defense (BC150640) and NIH/NCI (CA138488) during the conduct of the study. **H.C. Playa** also reports grant support from the METAvivor foundation during the conduct of the study. **D. Layman** reports support from the West Cancer Center (Memphis, TN) during the conduct of the study. The content is solely the responsibility of the authors and does not necessarily represent the official views of the National Institutes of Health or the Department of Defense.

Author contributions. R.I. Krutilina: Conceptualization, methodology development, investigation, figure preparation, writing, including review and editing. **H.C. Playa**: Methodology development, investigation, figure preparation, writing, including review and editing. The first two authors contributed equally and are listed in alphabetical order. **D.L. Brooks**: Conceptualization, methodology development, investigation, figure preparation, writing, including review and editing. **L.P. Schwab**: Methodology development, investigation. **D.N. Parke**: Methodology development, investigation, figure preparation. **D. Oluwalana**: Investigation and figure preparation. **D. Layman**: Investigation and figure

preparation. **M. Fan**: Data analysis and bioinformatics support. **D.L. Johnson**: Data analysis and bioinformatics support. **J. Yue**: Generation of research materials and methodology development. **H. Smallwood**: Investigation, data analysis, and figure preparation. **T.N. Seagroves**: Conceptualization, resources, supervision, funding acquisition, data analysis, and figure preparation, writing-original draft, and writing-review and editing.

Table 1. Cyclocreatine (cCr) IC_{50} values in PyMT ER-negative cells. IC_{50} values ± SEM were determined at 96 h as described in the methods. IC_{50} values for independent experiments were calculated using non-linear regression and variable slope fit in Prism 9.0. Results from independent experiments were averaged to report the mean (n=6, WT; n=6, HIF-1 KO; n= 4, EV; n=6, sh61).

HIF-1 WT	HIF-1 KO	EV	sh61 CKB KD
16.76 mM ± 4.47	15.44 mM ± 3.95	13.73 mM ± 4.33	16.43 mM ± 2.98

Table 2: Calculation of monotherapy IC_{50} values in human TNBC cell lines. IC_{50} values ± SEM were determined at 96 h as described in the methods. IC_{50} values for independent experiments were calculated using non-linear regression and variable slope fit in Prism 9.0. Results from independent experiments were averaged to report the mean (n=4 replicates per cell line per drug).

Cell Line	cCr IC_{50}, mM	Taxol IC_{50}, nM	DOX IC_{50}, nM
MDA-MB-468	19.15 ± 3.06	11.16 nM ± 2.94	343.6 ±126.6
BT549	22.38 ±1.47	3.82 ± 0.44	28.28 ± 3.68
MDA-MB-453	6.10 ± 1.48	6.03 ± 1.75	60.39 ± 11.53

Table 3: Combination indices calculated for human TNBC cell lines pairing cCr with either Taxol or DOX. Isobole studies were performed as described in the materials and methods; data representative of 2 independent assays are shown.

	Taxol @ IC_{50} + cCr @ IC_{30} Combination Indices (CI)		DOX @ IC_{50} + cCr @ IC_{30} Combination Indices (CI)	
Cell Line	$IC_{50, TAXOL}$ CI	$IC_{70,TAXOL}$ CI	$IC_{50, DOX}$ CI	$IC_{70, DOX}$ CI
MDA-MB-468	1.06	0.52	0.61	0.39
BT549	0.86	0.58	1.50	1.28
MDA-MB-453	0.95	2.18	0.77	1.40

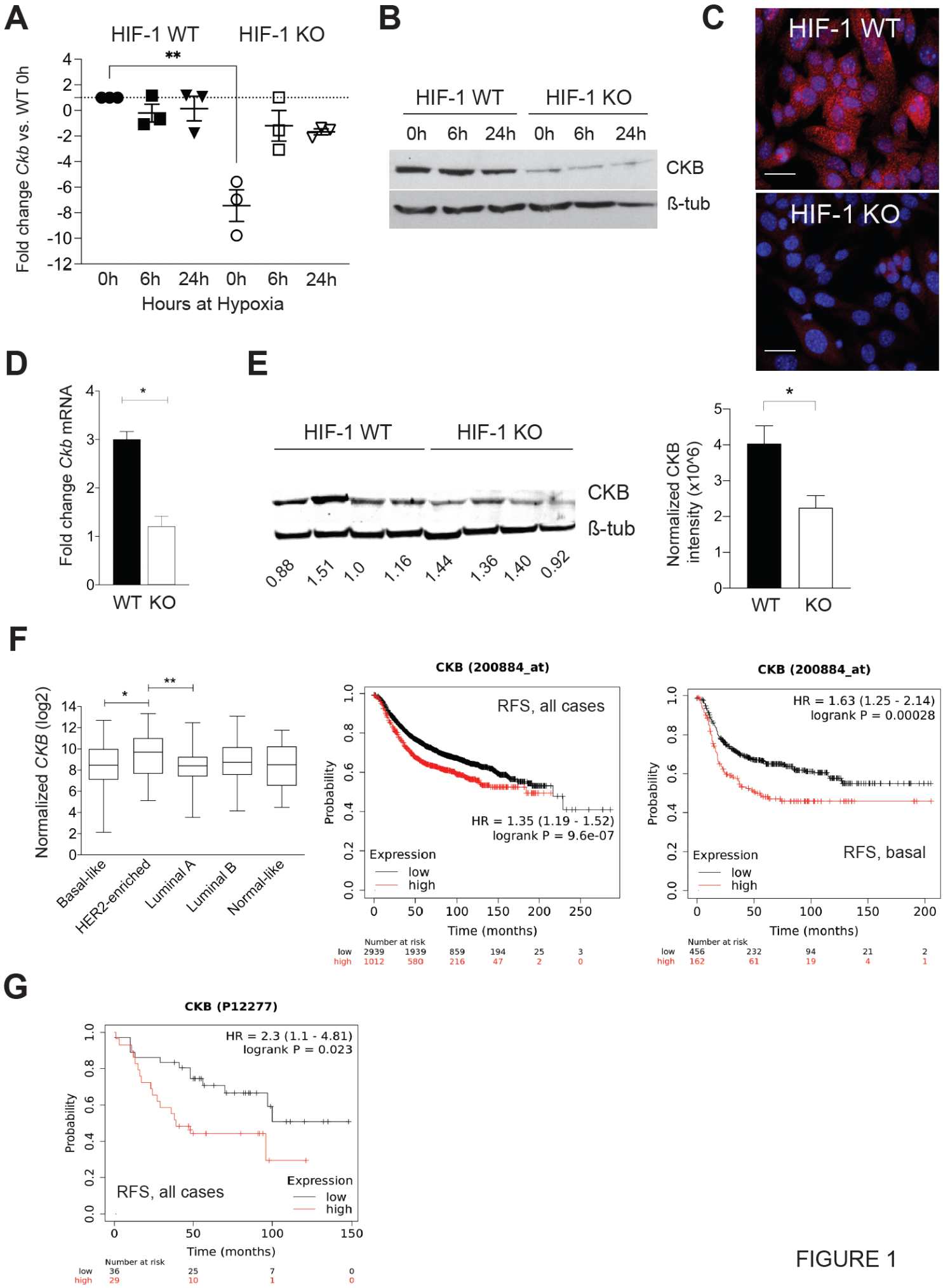
A
HIF-1 WT
HIF-1 KO
**
Fold change Ckb vs. WT 0h
4
2
0
-2
-4
-6
-8
-10
-12
0h 6h 24h 0h 6h 24h
Hours at Hypoxia
B
HIF-1 WT
HIF-1 KO
0h 6h 24h 0h 6h 24h
CKB
ß-tub
C
HIF-1 WT
HIF-1 KO
D
Fold change Ckb mRNA
*
WT KO
E
HIF-1 WT
HIF-1 KO
CKB
ß-tub
0.88 1.51 1.0 1.16 1.44 1.36 1.40 0.92
Normalized CKB intensity (x10^6)
*
WT KO
F
Normalized CKB (log2)
*
**
Basal-like
HER2-enriched
Luminal A
Luminal B
Normal-like
CKB (200884_at)
RFS, all cases
HR = 1.35 (1.19 - 1.52)
logrank P = 9.6e-07
Expression
low
high
Probability
Time (months)
Number at risk
low 2939 1939 859 194 25 3
high 1012 580 216 47 2 0
CKB (200884_at)
HR = 1.63 (1.25 - 2.14)
logrank P = 0.00028
RFS, basal
Expression
low
high
Probability
Time (months)
Number at risk
low 456 232 94 21 2
high 162 61 19 4 1
G
CKB (P12277)
HR = 2.3 (1.1 - 4.81)
logrank P = 0.023
RFS, all cases
Expression
low
high
Probability
Time (months)
Number at risk
low 36 25 7 0
high 29 10 1 0

FIGURE 1

FIGURE 2

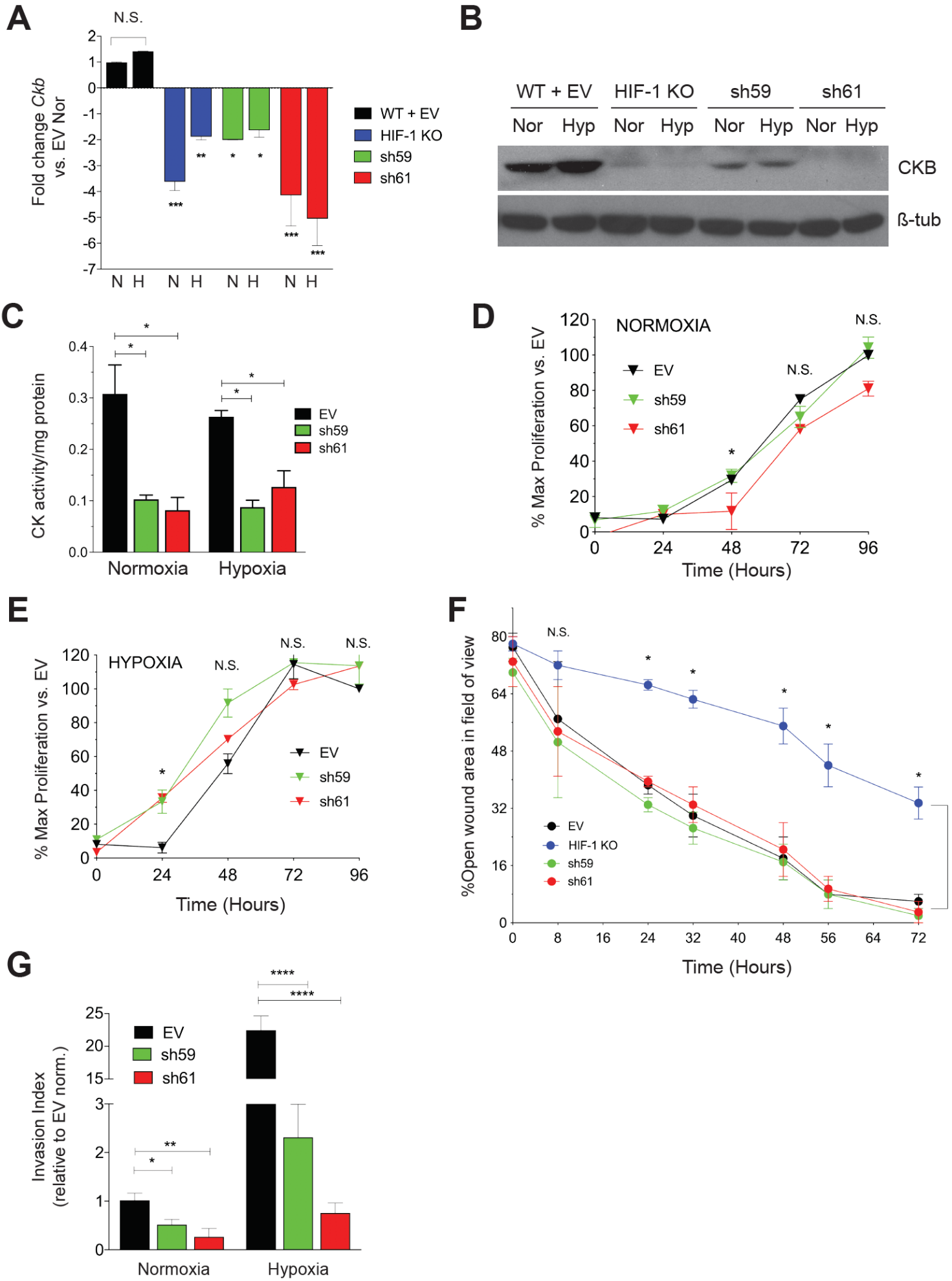
A
N.S.
Fold change Ckb vs. EV Nor
WT + EV
HIF-1 KO
sh59
sh61
N H N H N H N H
B
WT + EV
HIF-1 KO
sh59
sh61
Nor Hyp Nor Hyp Nor Hyp Nor Hyp
CKB
ß-tub
C
CK activity/mg protein
EV
sh59
sh61
Normoxia
Hypoxia
D
NORMOXIA
% Max Proliferation vs. EV
EV
sh59
sh61
N.S.
Time (Hours)
E
HYPOXIA
% Max Proliferation vs. EV
N.S.
EV
sh59
sh61
Time (Hours)
F
%Open wound area in field of view
N.S.
EV
HIF-1 KO
sh59
sh61
Time (Hours)
G
Invasion Index (relative to EV norm.)
EV
sh59
sh61
Normoxia
Hypoxia

FIGURE 3

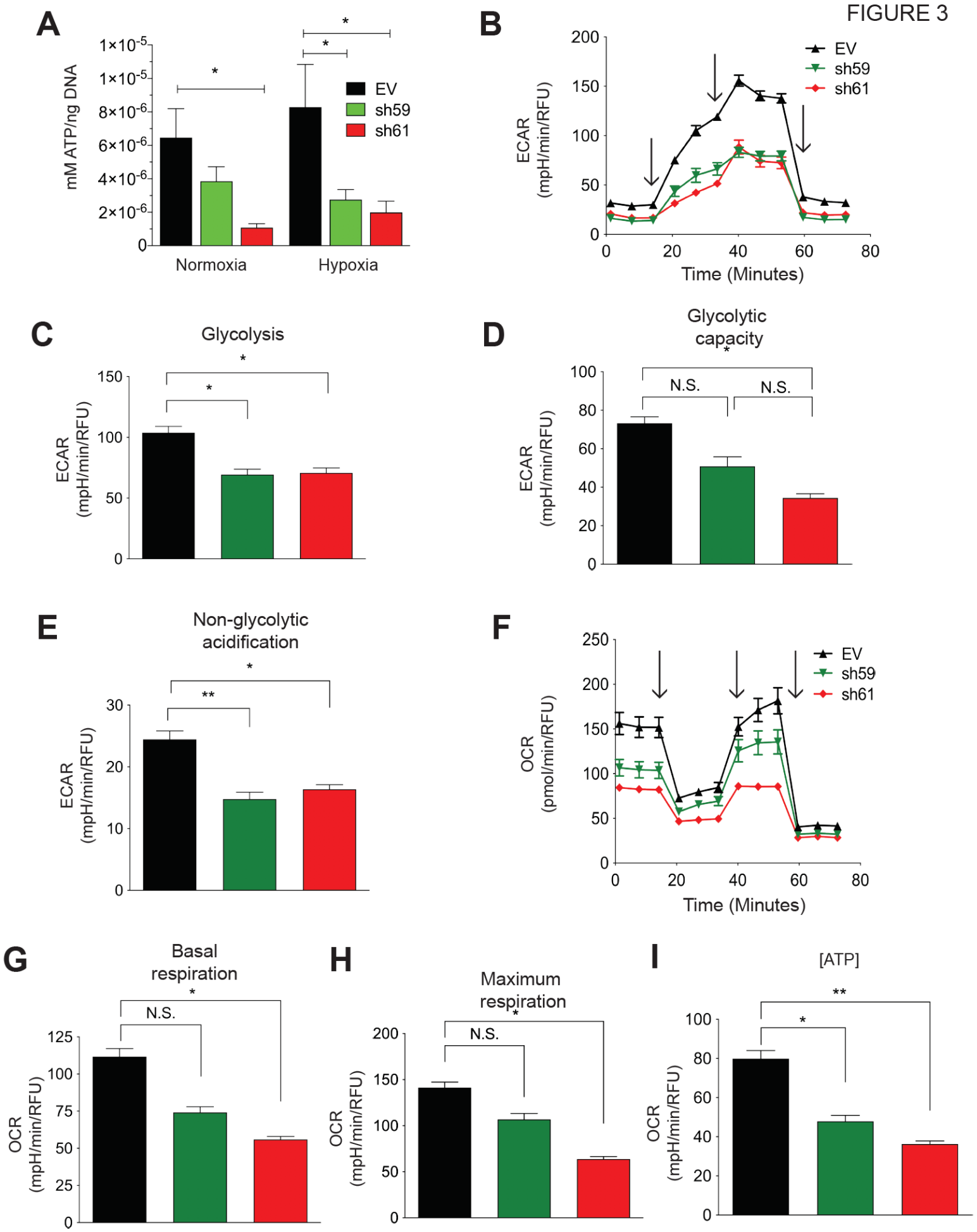
A
mM ATP/ng DNA
1×10-5
1×10-5
8×10-6
6×10-6
4×10-6
2×10-6
0
*
*
*
EV
sh59
sh61
Normoxia
Hypoxia
B
ECAR (mpH/min/RFU)
200
150
100
50
0
EV
sh59
sh61
0
20
40
60
80
Time (Minutes)
C
Glycolysis
ECAR (mpH/min/RFU)
150
100
50
0
*
*
D
Glycolytic capacity
ECAR (mpH/min/RFU)
100
80
60
40
20
0
*
N.S.
N.S.
E
Non-glycolytic acidification
ECAR (mpH/min/RFU)
30
20
10
0
*
**
F
OCR (pmol/min/RFU)
250
200
150
100
50
0
EV
sh59
sh61
0
20
40
60
80
Time (Minutes)
G
Basal respiration
OCR (mpH/min/RFU)
125
100
75
50
25
0
*
N.S.
H
Maximum respiration
OCR (mpH/min/RFU)
200
150
100
50
0
*
N.S.
I
[ATP]
OCR (mpH/min/RFU)
100
80
60
40
20
0
**
*

FIGURE 4

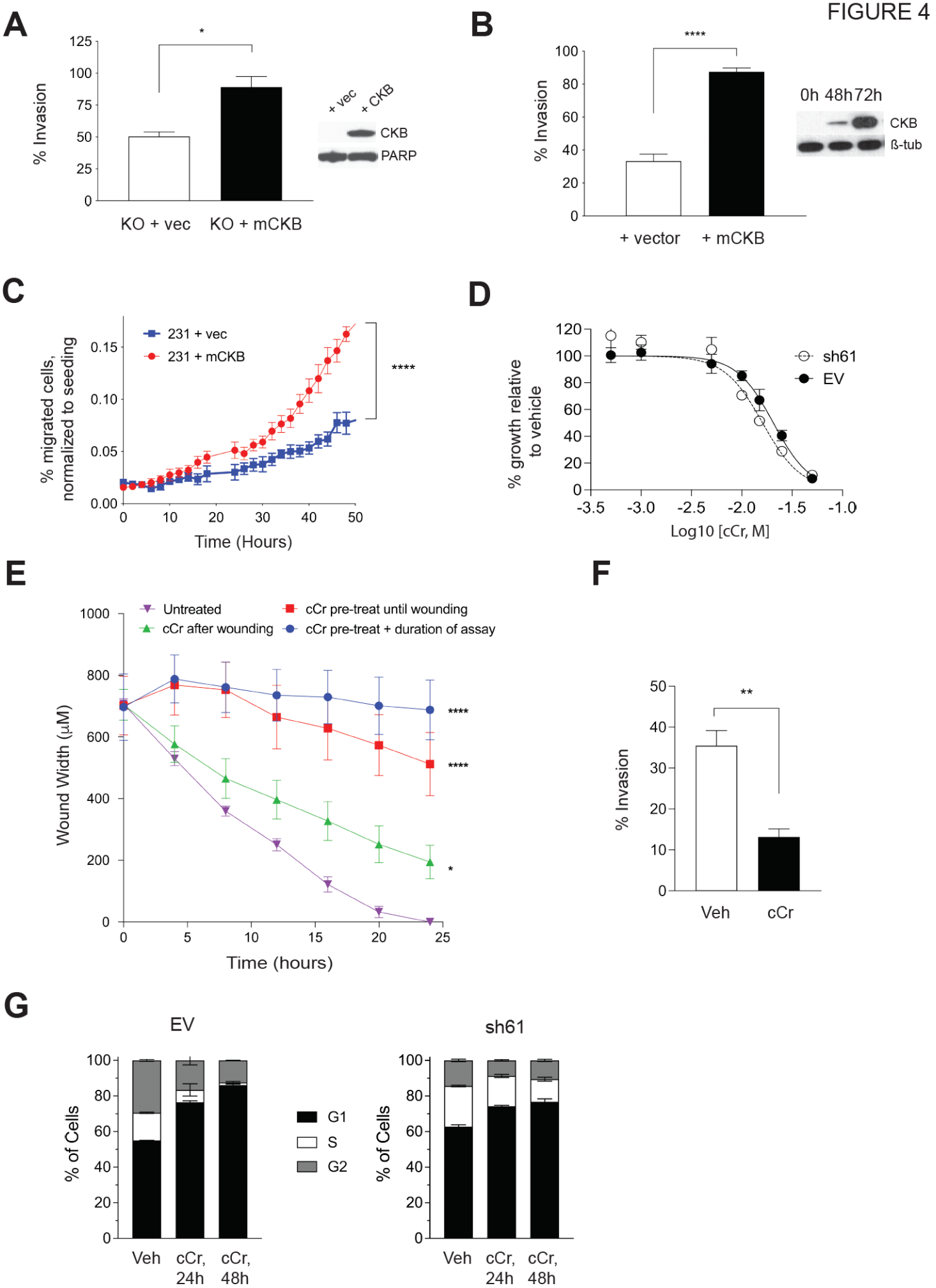
A
% Invasion
125
100
75
50
25
0
*
KO + vec
KO + mCKB
+ vec
+ CKB
CKB
PARP
B
% Invasion
100
80
60
40
20
0
****
+ vector
+ mCKB
0h 48h72h
CKB
ß-tub
C
% migrated cells, normalized to seeding
0.15
0.10
0.05
0.00
231 + vec
231 + mCKB
****
0
10
20
30
40
50
Time (Hours)
D
% growth relative to vehicle
120
100
80
60
40
20
0
sh61
EV
-3.5
-3.0
-2.5
-2.0
-1.5
-1.0
Log10 [cCr, M]
E
Untreated
cCr pre-treat until wounding
cCr after wounding
cCr pre-treat + duration of assay
Wound Width (μM)
1000
800
600
400
200
0
****
****
*
0
5
10
15
20
25
Time (hours)
F
% Invasion
50
40
30
20
10
0
**
Veh
cCr
G
EV
sh61
% of Cells
100
80
60
40
20
0
G1
S
G2
Veh
cCr, 24h
cCr, 48h

FIGURE 5

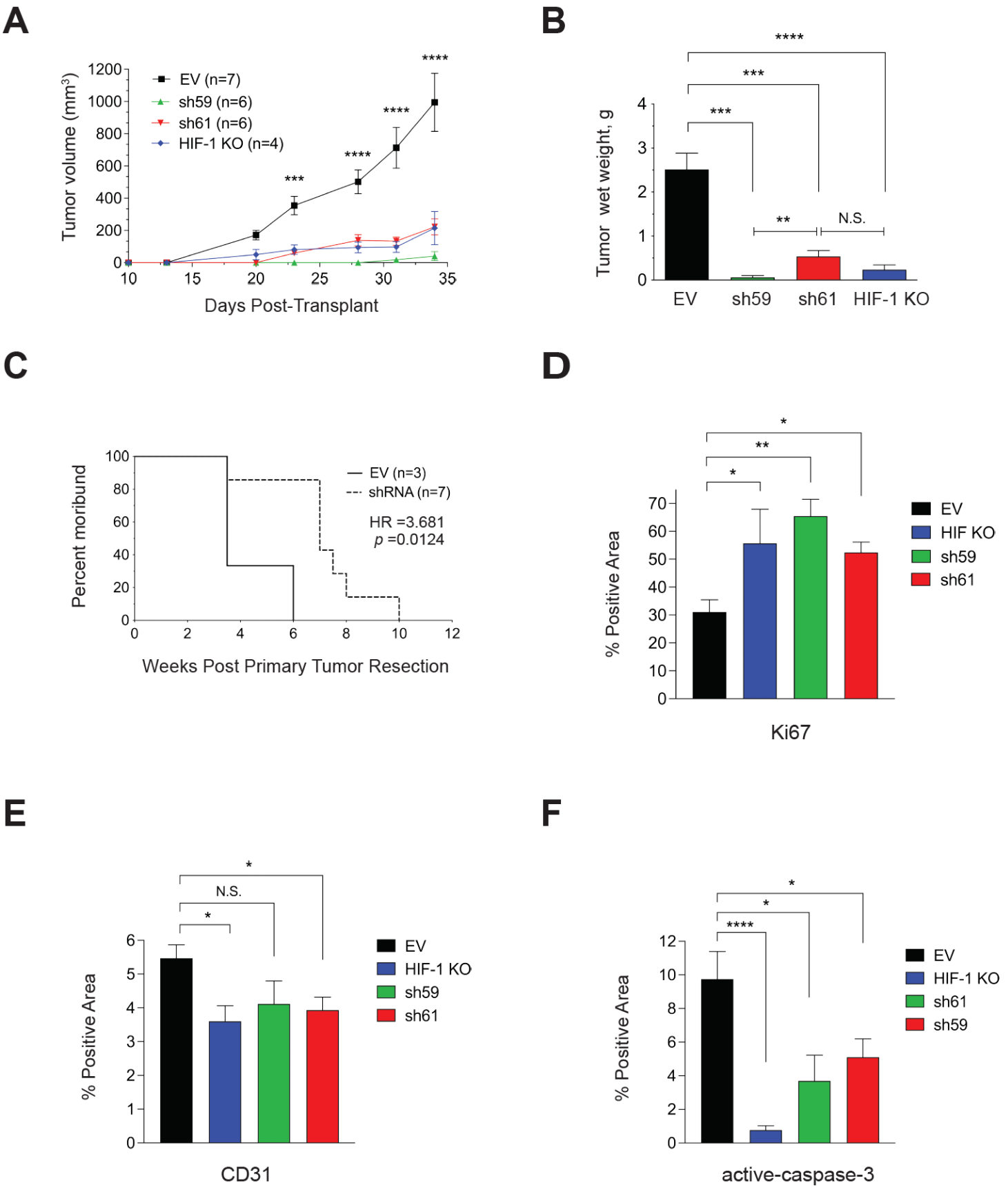
A
Tumor volume (mm³)
EV (n=7)
sh59 (n=6)
sh61 (n=6)
HIF-1 KO (n=4)
***
****
****
****
Days Post-Transplant
B
Tumor wet weight, g
****
***
***
**
N.S.
EV
sh59
sh61
HIF-1 KO
C
Percent moribund
EV (n=3)
shRNA (n=7)
HR =3.681
p =0.0124
Weeks Post Primary Tumor Resection
D
% Positive Area
*
**
*
EV
HIF KO
sh59
sh61
Ki67
E
% Positive Area
*
N.S.
*
EV
HIF-1 KO
sh59
sh61
CD31
F
% Positive Area
*
*
****
EV
HIF-1 KO
sh61
sh59
active-caspase-3

FIGURE 6

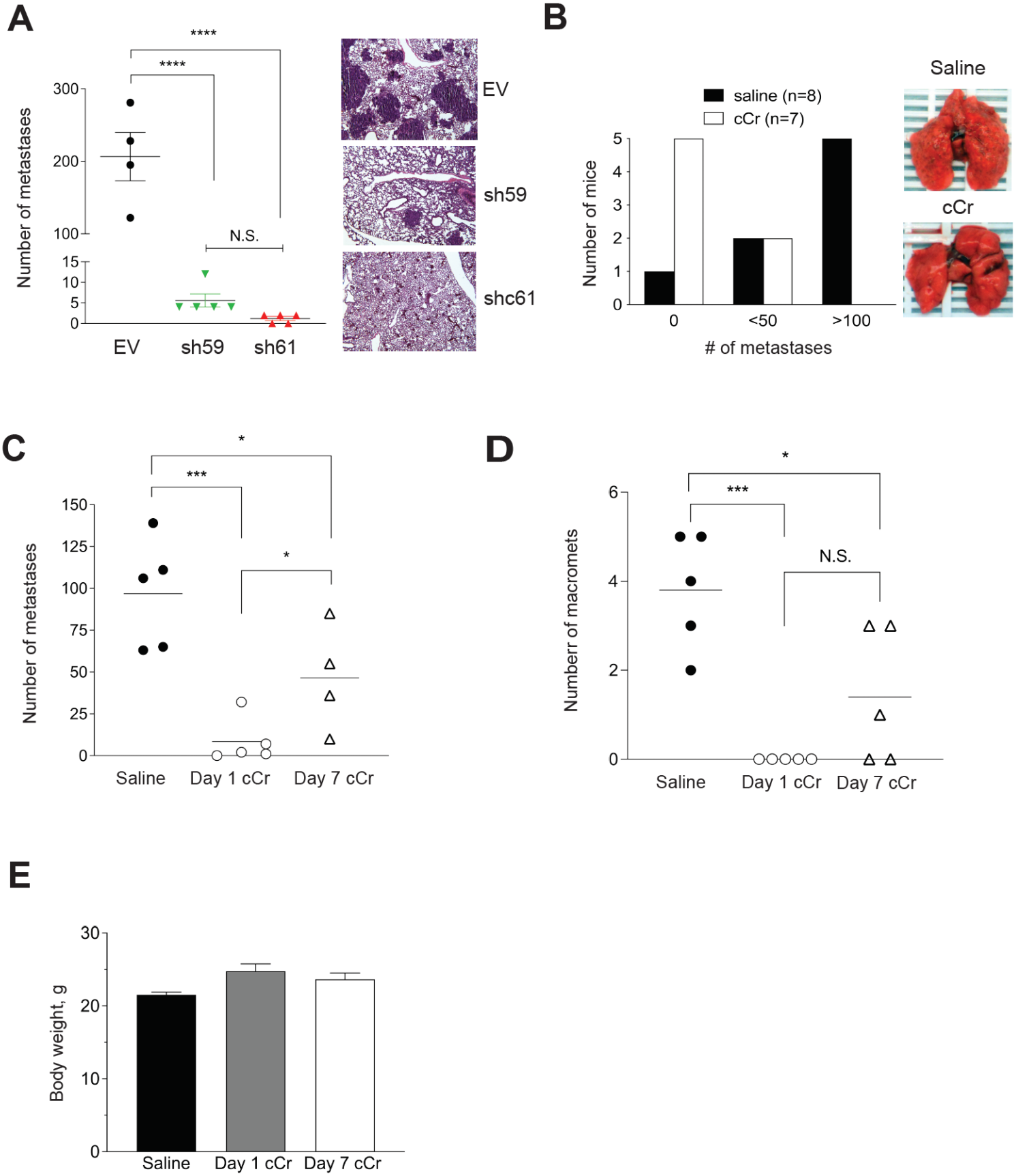
A
****
****
N.S.
Number of metastases
300
200
100
15
10
5
0
EV
sh59
sh61
EV
sh59
shc61
B
saline (n=8)
cCr (n=7)
Number of mice
5
4
3
2
1
0
0
<50
>100
# of metastases
Saline
cCr
C
*
***
*
Number of metastases
150
125
100
75
50
25
0
Saline
Day 1 cCr
Day 7 cCr
D
*
***
N.S.
Numberr of macromets
6
4
2
0
Saline
Day 1 cCr
Day 7 cCr
E
Body weight, g
30
20
10
0
Saline
Day 1 cCr
Day 7 cCr

FIGURE 7

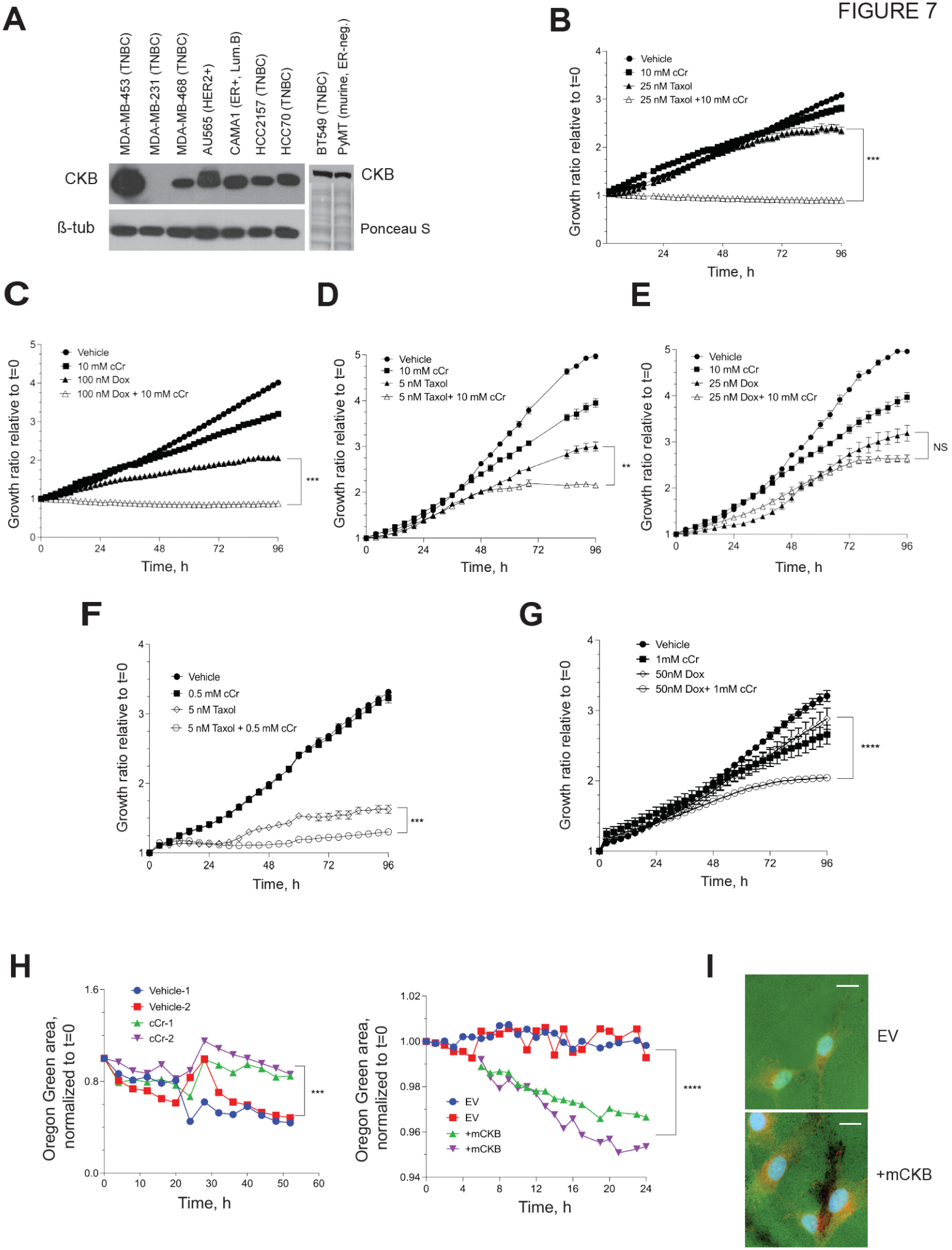
A
MDA-MB-453 (TNBC)
MDA-MB-231 (TNBC)
MDA-MB-468 (TNBC)
AU565 (HER2+)
CAMA1 (ER+, Lum.B)
HCC2157 (TNBC)
HCC70 (TNBC)
BT549 (TNBC)
PyMT (murine, ER-neg.)
CKB
ß-tub
CKB
Ponceau S
B
Vehicle
10 mM cCr
25 nM Taxol
25 nM Taxol +10 mM cCr
Growth ratio relative to t=0
Time, h
***
C
Vehicle
10 mM cCr
100 nM Dox
100 nM Dox + 10 mM cCr
Growth ratio relative to t=0
Time, h
***
D
Vehicle
10 mM cCr
5 nM Taxol
5 nM Taxol+ 10 mM cCr
Growth ratio relative to t=0
Time, h
**
E
Vehicle
10 mM cCr
25 nM Dox
25 nM Dox+ 10 mM cCr
Growth ratio relative to t=0
Time, h
NS
F
Vehicle
0.5 mM cCr
5 nM Taxol
5 nM Taxol + 0.5 mM cCr
Growth ratio relative to t=0
Time, h
***
G
Vehicle
1mM cCr
50nM Dox
50nM Dox+ 1mM cCr
Growth ratio relative to t=0
Time, h
****
H
Vehicle-1
Vehicle-2
cCr-1
cCr-2
Oregon Green area, normalized to t=0
Time, h
***
EV
EV
+mCKB
+mCKB
Oregon Green area, normalized to t=0
Time, h
****
I
EV
+mCKB

Figure 1. CKB expression in HIF-1 WT and KO PyMT cells and end-stage tumors, and CKB expression predicts poor prognosis in clinical datasets. A. Scatter plot of the mean fold-change ± SEM in *Ckb* mRNA levels relative to HIF-1 WT cells at normoxia. Each data point represents an independent qPCR assay, and the grand mean plus SEM is shown. B. PyMT cells were grown to 80% confluence and subjected to hypoxic culture for either 6 h or 24 h, or cells were continuously cultured at normoxia, such that the 0h sample was harvested on the same day as the 24 h hypoxic sample. A representative western blot for CKB or ß-tubulin (loading control) is shown. C. Immunostaining for CKB (red) in HIF-1 WT and KO cells, counterstained with DAPI. Images were captured at 630x magnification, and the scale bar indicates 20 μm. D. *Ckb* mRNA expression levels were compared in end-stage HIF-1 WT and KO tumors by qPCR. Data are expressed as the grand mean fold-change ± SEM between WT and KO tumors; the KO sample was set to a fold-change of 1.0 in each experiment. All data were first normalized for epithelial content based on *Krt18* (n=3 tumors/genotype/experiment). E. Western blotting for CKB comparing four independent tumors (at a volume of 500-750 mm^3) per HIF genotype. The top half of the blot was blotted for CKB and the lower portion was blotted for ß-tubulin. Blots were imaged on a LiCor Odyssey infrared imaging system and CKB expression was compared in HIF-1 WT versus KO tumors after normalization to ß-tubulin levels. The bar graph shows the normalized CKB intensity ± SEM per genotype. F. (Left) TCGA was queried for *CKB* mRNA expression levels among breast cancer subtypes defined by PAM50. Log_2-normalized *CKB* expression is plotted,

along with the 95% confidence interval and standard deviation. (Right) KM Plotter was used to plot the probability of RFS when patients were stratified by low or high expression of *CKB* (200884_at); plots are shown for either all breast cancer cases or for basal breast cancer cases only. G. RFS is lower when CKB protein levels (P12277) are high. All images were directly exported from the KM Plotter tool.

Figure 2. Effect of *Ckb* knockdown in PyMT cells upon cell growth and invasion.

A. The mean fold change ± SEM in *Ckb* expression levels in HIF-1 KO cells and in shRNA KD pools (sh59 or sh61) relative to EV measured by qPCR. Cells expressing the sh61 shRNA showed the greatest reduction in *Ckb* mRNA levels. B. PyMT cells were grown to 80% confluence and subjected to normoxic or hypoxia culture for 6 h and immunoblotted for CKB or ß-tubulin (loading control). Changes in CKB protein levels are consistent with changes observed by qPCR, with sh61 KD cells showing the greatest reduction in CKB expression. C. CK^{act} (activity/mg protein) was measured in whole-cell extracts prepared from PyMT EV, sh59, or sh61 cells cultured at normoxia or hypoxia (6 h). The data shown are representative of three biological replicate experiments. D-E. Growth curves of PyMT EV, sh59, or sh61 cells cultured at normoxia (D) or hypoxia (E) in growth medium supplemented with 2% FBS. Cell proliferation was measured in replicate plates at each time point (24, 48, 72, or 96 h) using the WST-1 assay. For both oxygen tensions, the grand mean of the percentage of proliferating cells relative to EV cells at t=0 h ± SEM is presented, calculated as the average of mean cell

number for n=3 technical replicates per time point per genotype per condition as observed over three biological replicate experiments. All data were analyzed by two-way ANOVA; N.S.= not significant. F. PyMT EV, HIF-1 KO, sh59 KD, and sh61 KD cells were seeded into 6-well dishes such that they would be 100% confluent the next day. Following wounding, the percentage of open wound area in each field of view was measured and expressed as a ratio per the total area of the field of view. Data were analyzed by two-way ANOVA with a Bonferroni correction post-test. Only HIF-1 KO cells showed defects in wound healing. Data are representative of three biological replicate experiments. G. The grand mean fold change in the invasion index after data were normalized to EV cells cultured at normoxia (fold change set to 1.0; n=3 three independent biological replicate experiments_. Data were analyzed by ANOVA with a Bonferroni post-test.

Figure 3. *Ckb* knockdown in PyMT cells reduces ATP levels and impairs both glycolysis and mitochondrial respiration.

A. PyMT EV, sh59, and sh61 cells were plated in triplicate and grown to 80% confluence prior to normoxic or hypoxic culture (24h). Cells were harvested, washed with ice-cold PBS, and immediately lysed on the plate for comparison of intracellular ATP levels, which was normalized among genotypes to total DNA content. The mean ATP concentration (mM) per ng of DNA ± SEM is shown (n=3 technical replicates per cell line/condition). The data shown are representative of three independent biological replicates. B-I. PyMT EV, sh59 *Ckb* KD, and sh61 *Ckb* KD cells were profiled for metabolic activity using Seahorse bioanalyzer assays (Glycolysis Stress or Mito Stress test kits) to measure changes in

parameters associated with either extracellular acidification (ECAR, panels B-E) or with mitochondrial respiration (the oxygen consumption rate, OCR, panels F-I). The arrows (B, F) indicate when injections occurred during the bioanalyzer assays. Changes were observed in ECAR over time (B), glycolysis (C), glycolytic capacity (D), non-glycolytic acidification (E), OCR over time (F), basal respiration (G), maximum respiration (H), and ATP-linked respiration (I) in sh61 *Ckb* KD cells. For some of the measured outputs, there were also significant changes observed in sh59 *Ckb* KD cells. Panels B and F are representative of three independent experiments. For panels C-E and G-I, the bar graphs represent the grand mean of three independent experiment means across n=6 technical well replicates per genotype per experiment. Each genotype of cells was randomly plated in different patterns for each independent experiment to minimize any potential effects of plate well location on measurements.

Figure 4. Ectopic expression of CKB in HIF-1 KO PyMT cells or in human MDA-MB-231 TNBC cells enhances cell invasion, but cCr treatment represses wound healing, invasion, and cell cycle progression.

A. The percentage of invading cells was compared between PyMT HIF-1 KO + vector control (+ vec) and PyMT HIF-1 KO + mCKB cells over three biological experiments; the grand mean ± SEM is shown. The insert shows CKB expression by western blotting relative to total PARP (loading control). B. The percentage of invading cells in MDA-MB-231 TNBC cells transfected with vector alone (+ vector) or with mCKB (+ mCKB); cells were plated for invasion assays 72 h post-

transfection when CKB levels were maximally expressed (western blot insert, ß-tubulin loading control). C. Chemotaxis assays were performed in transiently transfected MDA-MB-231 cells using the IncuCyte ClearView system. The mean percentage of migrated cells/total cells seeded was compared between genotypes over time during chemoattraction to 10% FBS. Data are representative of two independent experiments. F. PyMT EV cells were seeded in an invasion assay in which cells in the upper chamber were exposed to either vehicle or to 25 mM cCr and then cultured for 48 h. G. PyMT EV or sh61 cells were treated with 25 mM cCr for either 24 h or 48 h and cell cycle analysis was performed by PI staining to assay for changes in cell cycle progression. The mean ± SEM is shown for each phase of the cell cycle (n=3 technical replicates/genotype/time point). Data are representative of three independent experiments.

Figure 5. Tumor cell-intrinsic CKB promotes PyMT primary tumor growth and lung metastasis *in vivo* and deletion of CKB in the tumor epithelium improves overall survival.

A. Growth rate over time after transplantation of PyMT EV, HIF-1 KO, sh59 KD, and sh61 KD cells into the inguinal mammary fat pad of female FVB/Nj recipients. Mean tumor volume ± SEM is shown. B. All tumors harvested at day 34 from panel A were weighed to determine the mean wet weight (g) ± SEM at experiment endpoint. Data in A-B are representative of two independent experiments. C. The impact of *Ckb* expression in the PyMT tumor epithelium on the survival of recipients following tumor resection. Mice implanted with PyMT cells (EV or either

shRNA KD construct) were subjected to primary tumor resection and allowed to survive post-resection until moribund due to lung metastasis. Mice were removed from the study when they were panting due to lung metastasis, or if bodyweight decreased by >15%. The morbidity hazard ratio (HR) is 3.68 times higher when FVB/Nj recipients bear *Ckb* WT tumors (n=3 mice for EV and n=7 total mice for CKB shRNA knockdown, representing either sh59 KD or sh61 KD tumors). D-F Immunostaining of PyMT EV (n=5 tumors), HIF-1 KO (n=4 tumors), sh59 KD (n=4 tumors) or sh61 KD (n=5 tumors) sections to enumerate Ki67 (D), CD31 (E) or activated-caspase 3 (F). The mean ± SEM of the percentage (%) of the positive area is reported for each genotype.

Figure 6. Knockdown of *Ckb* in the PyMT tumor epithelium or systemic cCr therapy decreases lung metastasis burden.

A. PyMT EV, sh59 KD, or sh61 KD cells were injected into the tail vein of female FVB/Nj recipients. After 21 days, mice were euthanized and lungs harvested for metastasis evaluation after lung inflation through the trachea with PBS. The number of metastases was compared across genotypes; the scatter plot shows the burden of individual lungs per genotype, the mean and the SEM are shown. Corresponding H&E--stained images of lungs representative of the genotype mean are shown at 400x magnification. Data are representative of two independent experiments. B. EV PyMT cells were injected into the tail vein of female FVB/Nj recipient mice. The next day, treatment with either vehicle (saline, IP, daily) or cCr (1g/kg in saline, IP, daily) was initiated. After 21 days, the mice

were euthanized and the lungs harvested after inflation with PBS. The total number of surface metastases was counted under a dissecting scope. A majority of the mice treated with cCr (5 of 7) did not develop detectable metastases, whereas 2 mice in each cohort (2/8, saline and 2/7, cCr) developed fewer than 50 metastases. Only in the saline group did most mice develop metastases throughout the lung with >100 lesions present (5/8 mice; data are significant by Chi-square analysis ($\chi 2$= 7.634, p=0.022). Images of whole lungs photographed immediately post-dissection are shown. C-D. Comparison of total metastases present per lung (C), or the number of macro-metastases per lung (D) when mice are treated with vehicle, when cCr is administered at either day 1 or when cCr therapy begins at day 7 post-tail vein injection of PyMT EV cells. All lungs were harvested at day 21 post-injection. E. The mean bodyweight of the mice treated with cCr from panels C-D.

Figure 7. Cyclocreatine is synergistic with or additive to conventional chemotherapies, and cyclocreatine inhibits the formation of breast tumor cell invadopodia.

A. (Left) Western blotting for endogenous CKB protein in a panel of human breast cancer cell lines; ß-tubulin is used as a loading control. (Right) Western botting for CKB protein in BT549 TNBC cells in a separate blot. BT549 TNBC cells express similar levels of CKB protein as PyMT HIF-1 WT cells; loading for this blot is indicated by Ponceau S staining. B-G. The growth ratio (all treatments were normalized to their respective t=0 cell density) over time when human MDA-MB-

468 TNBC cells (B-C), BT549 TNBC cells (D-E), or MDA-MB-453 cells (F-G) are cultured in the presence of vehicle, cCr alone, or cCr with Taxol (B, D, F) or doxorubicin (C, E, G), for 96 h and imaged in the IncuCyte S3 live-cell imager. H. Loss of Oregon Green-conjugated gelatin was measured in the S3 live-cell imager over time after seeding cells onto gelatin-coated coverslips in the presence of an MMP inhibitor, and replacement of growth medium with or without cCr as described in the methods. Quantification data over time is shown for vehicle-treated versus cCr-treated BT549 cells (H, left panel) or for MDA-MB-231 empty vector (EV) or MDA-MB-231 +mCKB cells (H, right panel). Two coverslips were measured simultaneously across all areas of each coverslip/well per experiment. Data are representative of three independent experiments. I. Example immunostaining images for invadopodia assay coverslips at experimental endpoint stained with cortactin (red) and DAPI (cell nuclei); 630x magnification, scale bar represents 20 μM. All images were captured on the Nikon Ti2 ECLIPSE system with identical laser and exposure settings.

Supplementary Tables

Table S4. Primers and Roche Universal Probe Library (UPL) FAM-labeled probes utilized in real-time PCR assays. All assays were designed using the Roche Universal ProbeLibrary Assay Design Center.

Gene	Forward Primer	Reverse Primer	UPL ID
Ckb (murine)	gcaagcacaggcatccat	cgcagcttctgcgtattatg	70
CKB (human)	cctgcccagaaatgaagc	gcactgcccaggcaataa	38
Ints3 (murine)	gtggctgttattgactctgcac	caggttccccatcatcacat	17
Krt18 (murine K18)	agatgacaccaacatcacaagg	cttccagaccttggacttcct	78
PPIA (Cyclophilin A)	atgctggacccaacacaaat	tctttcactttgccaaacacc	48

Table S5. Primary antibody source and dilution factors utilized in western blotting, immunofluorescence (IF) staining of cultured cells and DAB-based immunohistochemistry (IHC) staining of tumor tissues.

Antibody	Source and Catalog #	Dilution	Purpose
anti-CKB	AbCAM (#ab88746)	1:5,000	western
anti-ß-tubulin	AbCam (#(#ab6046)	1:10,000	western
anti-HIF-1α	Novus Biologicals (#NB100-479)	1:5,000	western
anti-PARP	Cell Signaling Technology (#9542)	1:5,000	western
anti-CKB	ThermoFisher (PA5-21382) or Santa Cruz, sc-271531)	1:500	IF, cells
anti-alpha tubulin	ThermoFisher (#62204)	1:250	IF, cells
anti-cortactin	Millipore (#05-0180)	1:700	IF, cells
anti-mouse AlexaFluor-488	LifeTech (#A21202)	1:400	IF, cells
anti-rabbit AlexaFluor-594	LifeTech (#A21203)	1:400	IF, cells
anti-rabbit-IgG-Biotin-X	LifeTech (#A16027)	1:400	IF, cells
Strepavidin-AlexaFlour-594	LifeTech (#S11227)	1:400	IF, cells
anti-Ki67	AbCAM (#ab-15580)	1:750	IHC
anti-CD31	Cell Signaling Technology (#77699)	1:100	IHC
anti-activated caspase3	Cell Signaling Technology (#9661)	1:100	IHC

Table S6. Primers used in chromatin immunoprecipitation (ChIP) assays in murine PyMT tumor cells and in human MCF-7 cells.

Genomic Region	IP Antibody	Forward Primer	Reverse Primer
-258 *CKB*	HIF-1α	gatgaacccaagcgtcctc	agacctcgaggccgaaac
-935 *CKB*	HIF-1α	attgctgggtcacggagtt	tacccccaacactcccagat
-1869 *CKB* non-HRE	HIF-1α	ttcaggttttgtggggtagc	ctgttccaagccagcatttt
-1326 *Ckb*	HIF-1α	cagggctgttctggactctc	cctcacaagtgctgggatta
-1835 *Ckb*	HIF-1α	tgcctcctgtgcacttttt	agcctagcttcagagaactaa tgg
-510 *Ckb* non-HRE	HIF-1α	cttggcggtgttccttagag	caggccatatcctcaagagc
EPO	HIF-1α	gctggcctctggctctcatgg	cagggttggcagctgccttact g
Vegf	HIF-1α	ctggcttcagttccctggcaacat ctct	cctggggtgaatgggatcctct gg

Table S7. *Ckb* shRNA targeting sequences obtained from The RNAi Consortium (TRC) library purchased through Open Biosystems.

Clone ID	Clone Name	Target Sequence
TRCN0000024659	NM_021273.2-300s1c1	cgacgtattcaaggacctctt
TRCN0000024660	NM_021273.2-288s1c1	cgaggagagttacgacgtatt
TRCN0000024661	NM_021273.2-708s1c1	gcacaatgacaataagacttt

FIG. S1

A

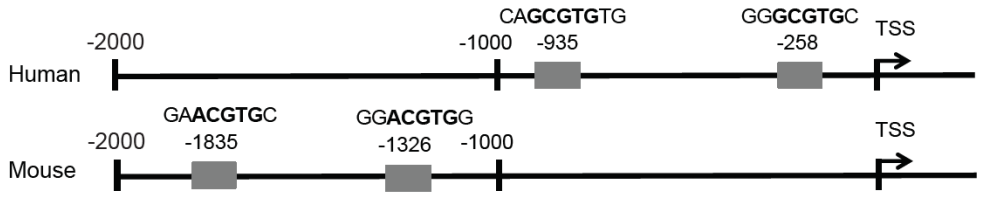
Human
-2000
-1000
CAGCGTGTG
-935
GGGCGTGC
-258
TSS
Mouse
-2000
GAACGTGC
-1835
GGACGTGG
-1326
-1000
TSS

B

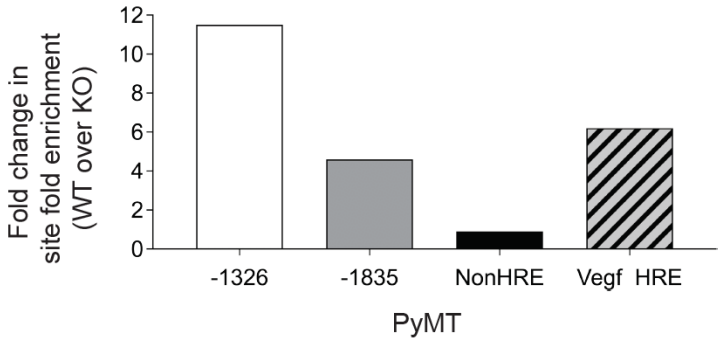
Fold change in site fold enrichment (WT over KO)
12
10
8
6
4
2
0
-1326
-1835
NonHRE
Vegf HRE
PyMT

C

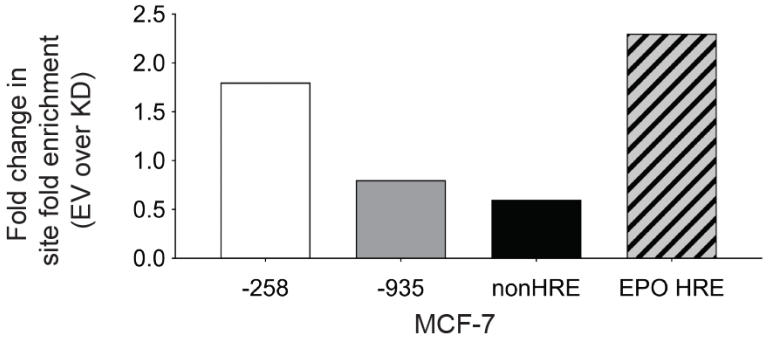
Fold change in site fold enrichment (EV over KD)
2.5
2.0
1.5
1.0
0.5
0.0
-258
-935
nonHRE
EPO HRE
MCF-7

D

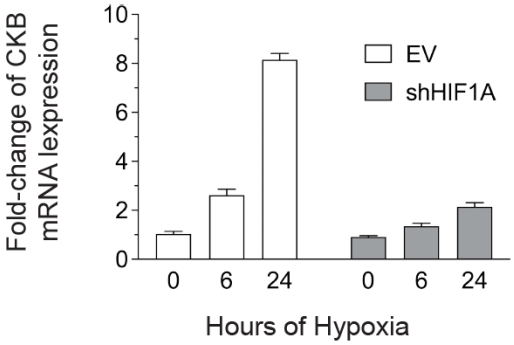
Fold-change of CKB mRNA lexpression
10
8
6
4
2
0
EV
shHIF1A
0
6
24
0
6
24
Hours of Hypoxia

FIG. S2

A

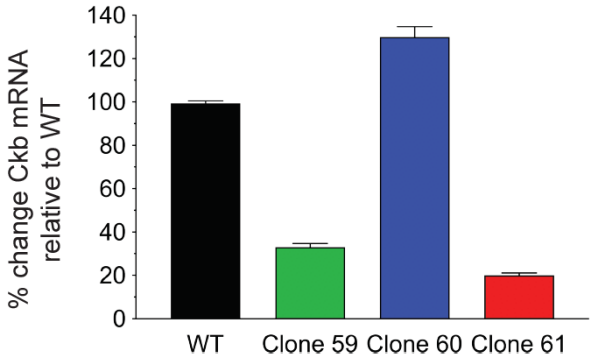
% change Ckb mRNA relative to WT
140
120
100
80
60
40
20
0
WT
Clone 59
Clone 60
Clone 61

B

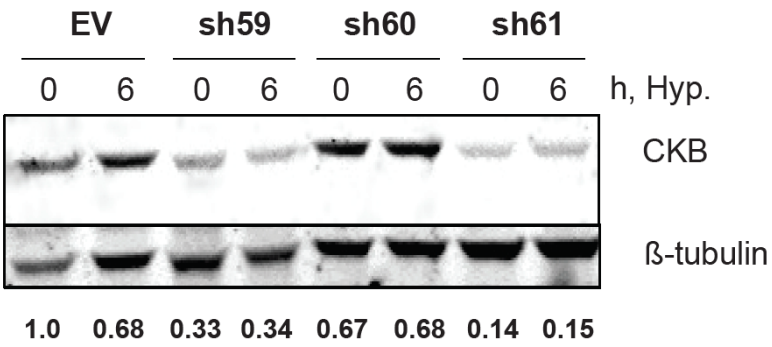
EV
sh59
sh60
sh61
0 6 0 6 0 6 0 6
h, Hyp.
CKB
ß-tubulin
1.0 0.68 0.33 0.34 0.67 0.68 0.14 0.15

C

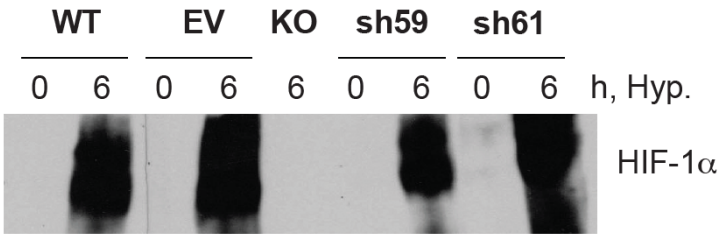
WT
EV
KO
sh59
sh61
0 6 0 6 6 0 6 0 6
h, Hyp.
HIF-1α

FIG. S3

A

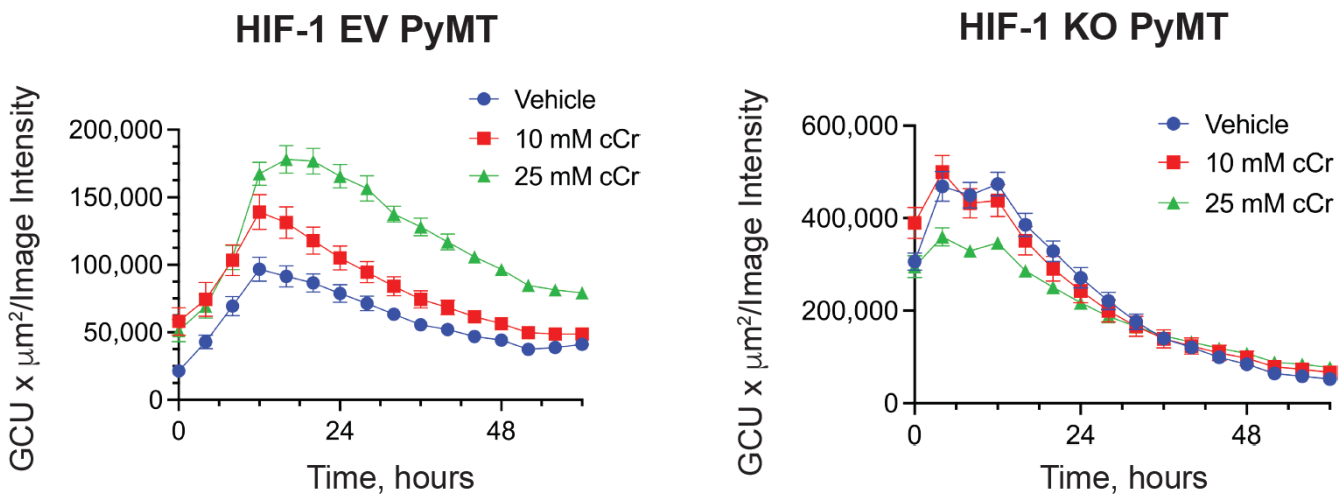
HIF-1 EV PyMT
GCU x µm²/Image Intensity
200,000
150,000
100,000
50,000
0
0
24
48
Time, hours
Vehicle
10 mM cCr
25 mM cCr
HIF-1 KO PyMT
GCU x µm²/Image Intensity
600,000
400,000
200,000
0
0
24
48
Time, hours
Vehicle
10 mM cCr
25 mM cCr

B

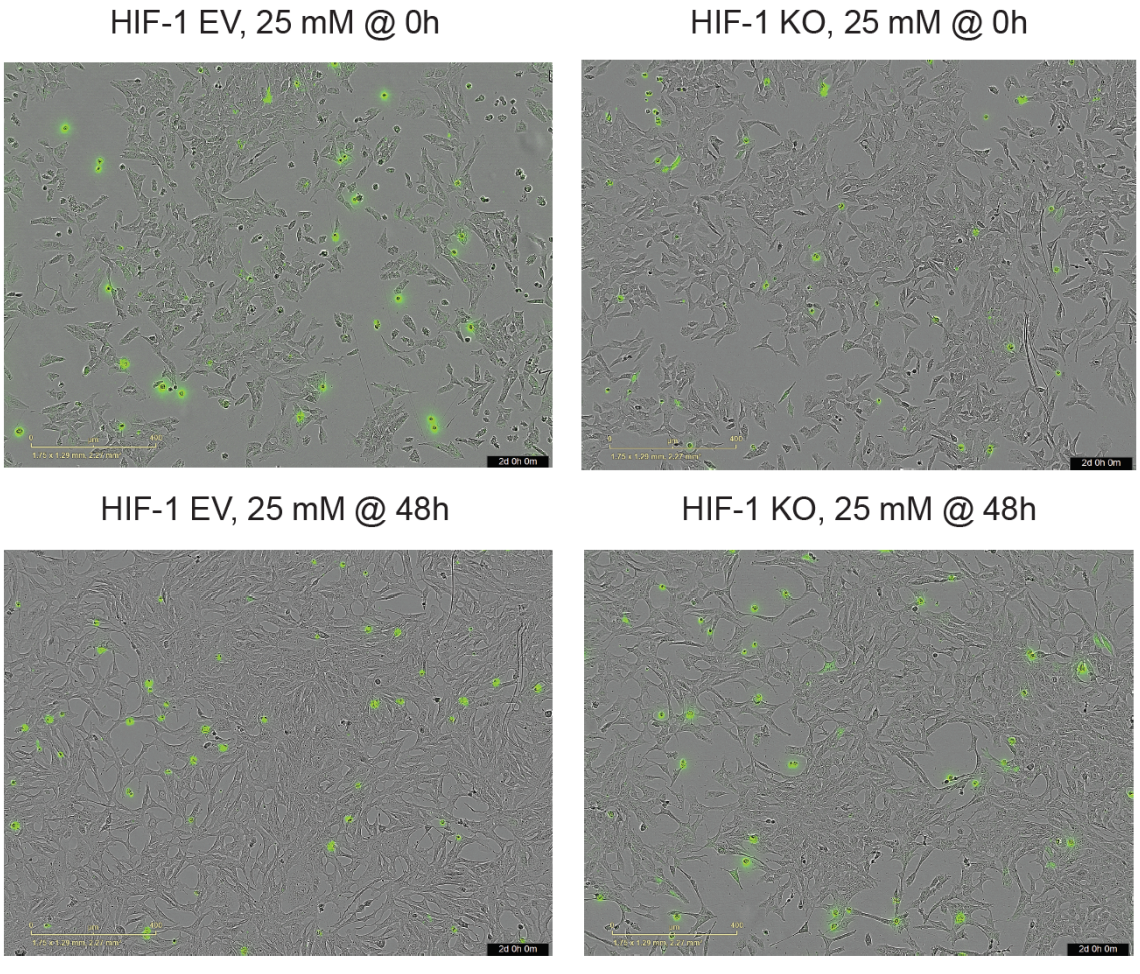
HIF-1 EV, 25 mM @ 0h
HIF-1 KO, 25 mM @ 0h
HIF-1 EV, 25 mM @ 48h
HIF-1 KO, 25 mM @ 48h

FIGURE S4

A

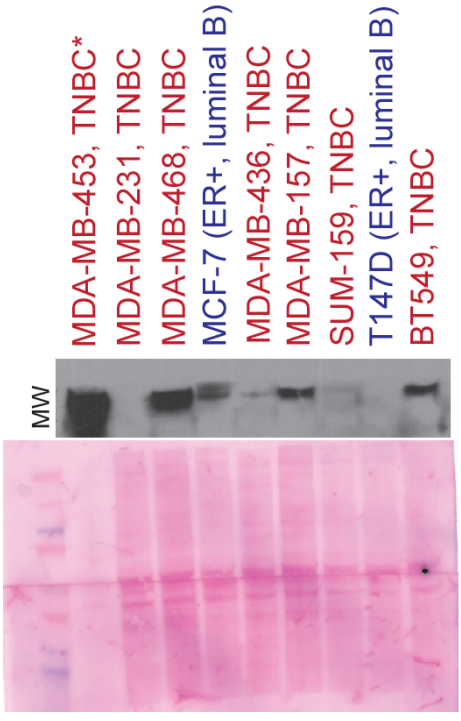

* TOP half blot probed for CKB

*MDA-MB-453 cells underloaded by 5-fold due to high levels of expression

FIG. S5

A

BT549, vehicle

BT549 + cCr

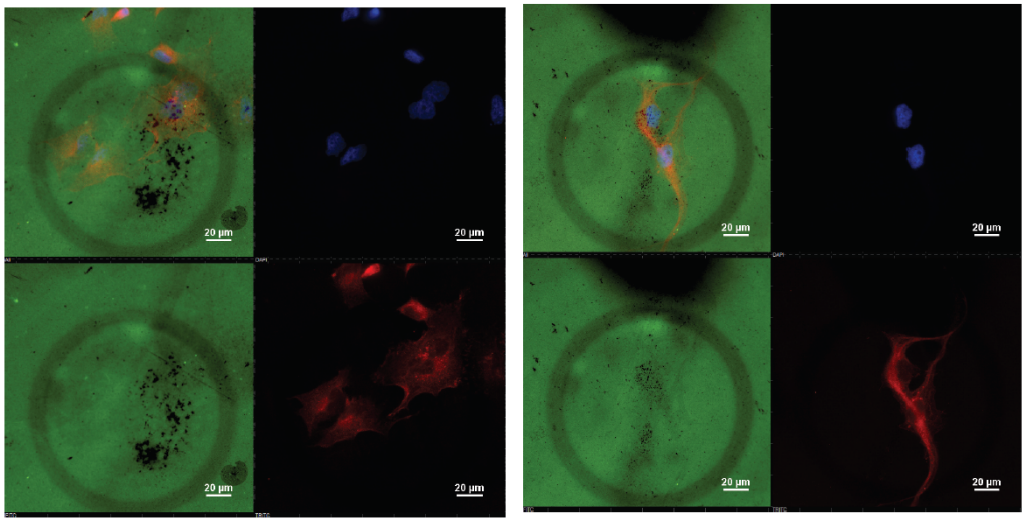

gelatin
cortactin
DAPI

B

231 cells +mCKB

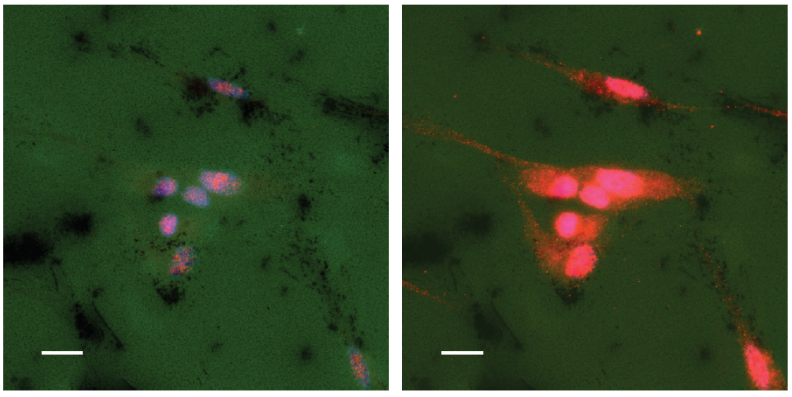

gelatin
mCKB
DAPI

short exposure

long exposure

FIG. S6

468, vehicle

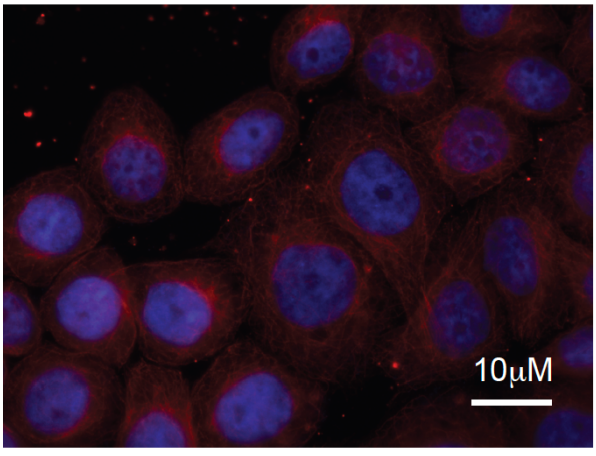

468, Taxol

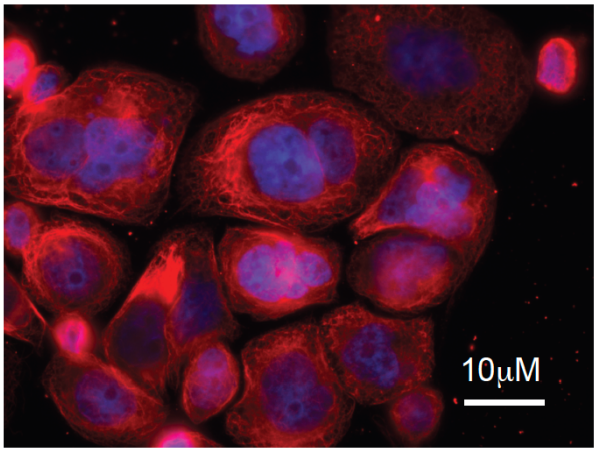

468 + cCr

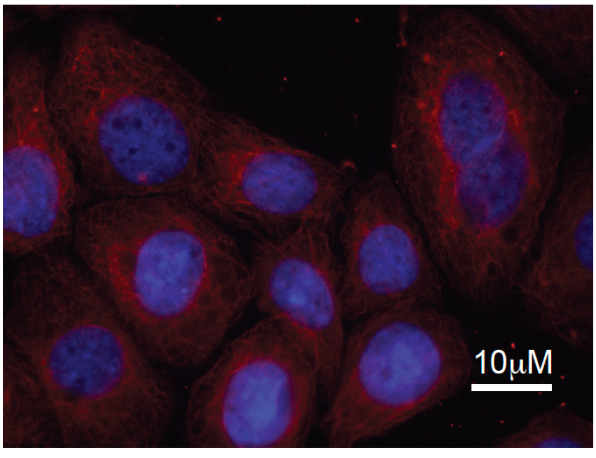

468 + Taxol + cCr

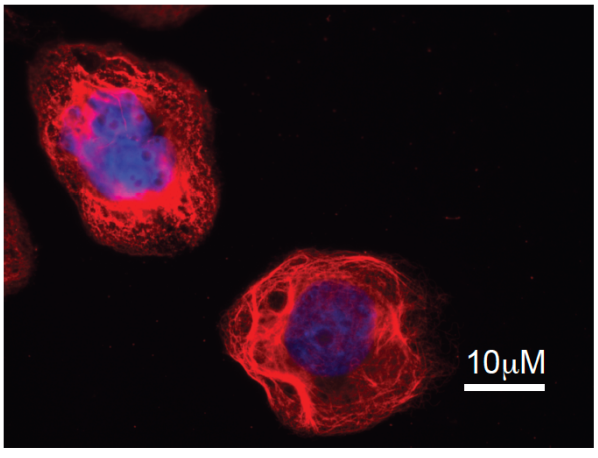

Supplementary Figure S1. Chromatin immunoprecipitation (ChIP) analysis of the *Ckb/CKB* proximal promoter in PyMT and MCF-7 breast cancer cells.

A. A schematic representation of two putative hypoxia response elements (HREs) identified by the JASPAR database in either the mouse (*Ckb*) or the human (*CKB*) gene proximal promoter. B-C. All cells were cultured to ~80% confluence and then exposed to hypoxia for 24 h (0.5% O_2) prior to the isolation of chromatin. ChIP assays were performed with antibodies to HIF-1α antibodies (AbCAM, cat# H1alpha67, ab1). and qPCR was conducted on the isolated DNA to determine HIF1α recruitment. Binding enrichment \epresented at each HRE site is expressed as the fold change between HIF-1 wild type PyMT cells (B), or MCF-7 empty vector (EV) (C) cells relative to either HIF-1 KO PyMT cells (B) or MCF-7 shHIF1A knockdown (KD) cells (C), respectively, after normalizing to the IgG control. As internal assay controls for the PyMT cells, ChIP was also performed for a known HRE in the mouse *Vegf* promoter [57] or using an intron within *Ckb* with no identified HRE sites. As internal assay controls for MCF-7 cells, ChIP for HIF-1α was performed in a known HRE site in the *EPO* 3' UTR [58], or using an intron within *CKB* with no identified HRE sites. D. *CKB* mRNA levels were measured by qPCR in MCF-7 EV and shHIF1A cells cultured for 0, 6 or 24 h of hypoxia. The fold change in *CKB* expression was calculated after normalization for loading to *PPIA*.

Supplementary Figure S2. Comparing gene knockdown efficiency of *Ckb* shRNA constructs in PyMT cells.

A. HIF-1 WT PyMT cells were transfected with three different pLKO.1-puro-shRNA targeting viral backbones to screen for deletion efficiency at the mRNA level by qPCR (n=4 technical replicates/cell line) when cells were cultured at normoxia. B. Western blot analysis of CKB protein levels using replicate plates from (A), along with EV PyMT cells (expressing empty pLKO.1-puro); ß-tubulin is used as a loading control. The EV 0 h hypoxia sample was set to 1.0 and ImageJ was used to evaluate densitometry values of CKB protein. C. Western blotting of HIF-1α in WT parental, HIF-1 WT + EV (EV), HIF-1 KO parental, or *Ckb* sh59 KD and sh61 KD cells cultured at normoxia (excluding HIF-1 KO) or for 6h at hypoxia following transduction with pLKO.1-puro-based recombinant lentiviruses, and the selection of stable shRNA KD pools. Western blots for HIF-1α were performed as detailed in [13]. HIF-1α is present as a ubiquitinylated protein smear after exposure to hypoxia.

Supplementary Figure S3. CytoTox Green assays to measure cell viability after exposure to 15 mM or 25 mM cCr for up to 48h.

A. PyMT EV cells used in wound healing, invasion, and cell cycle progression experiments as presented in Figure 4, or HIF-1 KO cells, were grown in 2% FBS (standard growth medium) and then exposed to either 15 mM cCr (the ~IC_{50}) or 25 mM cCr in the presence of CytoTox Green reagent. The intensity of CytoTox Green dye incorporated by dead cells was enumerated over time using the IncuCyte S3

live-cell imager. B. Although HIF-1 EV cells appeared to be more sensitive to cCr treatment over time (A), they also had a higher basal level of cell death on a per cell basis than HIF-1 KO cells at t=0 h. Example well scan images for each genotype are shown at t=0 h (1 h after addition of CytoTox and when scanning began) and at t=48 h (experimental endpoint). Overall, the images indicated that on a per cell level, CytoTox Green positive cells are approximately equivalent between PyMT EV and PyMT HIF-1 KO genotypes in the presence of 25 mM cCr.

Supplementary Figure S4. Comparison of CKB levels in additional human breast cancer cell lines. A. Western blot comparing CKB expression between TNBC cells (red font: MDA-MB-453, MDA-MB-231, MDA-MB-468, MDA-MB-436, MDA-MB-157, SUM-59, BT-549) and two ER-positive luminal B models (blue font), MCF-7 cells, known to express CKB, and T47D cells. Of note, the MDA-MB-453 sample was underloaded by ~5-fold due to high levels of expression (refer to Figure 7A); for the other samples, loading is equivalent as shown by Ponceau S staining of the whole blot; however, only the top half of the blot was probed for CKB.

Supplementary Figure S5. Immunostaining of invadopodia coverslips at the experimental endpoint.

A. Example images of coverslips used for invadopodia assays for the BT549 TNBC cell line. During invadopodia formation, BT549 cells were exposed to either vehicle (left panel) or to 25 mM cCr (~IC_{50}; right panel) for 48-50 h (green=gelatin;

red=cortactin; blue=DAPI). Scale bar represents 20 μM. B. MDA-MB-231 cells ectopically expressing mCKB readily formed invadopodia (Figure 7). At the study endpoint, coverslips containing invadopodia were immunostained with CKB antibodies. The image represents the same area imaged with either a short or a long exposure time in the red channel with the green laser intensity also minimized. In the longer exposure image, mCKB can be found along the periphery of the cell and in the cell projections overlapping with invadopodia, as well as in the cytoplasm and in the nucleus; the scale bar represents 20 μM.

Supplementary Figure S6. Tubulin networks following Taxol treatment in combination with cCr.

MDA-MB-468 cells were plated into ibidi multi-chamber well polymer slides, allowed to adhere for 48 h, treated with either 20 mM cCr, 10 nM Taxol, or both drugs for 48 h, then washed, fixed, and immunostained with alpha-tubulin (red) and counterstained with DAPI. All images were captured on a Nikon ECLIPSE Ti2 microscope at the same laser intensities and exposure times at 400x magnification; scale bars represent 10 μM.